Postprint

Quantitative phase-field modeling of faceted crystal dissolution processes

by N. Prajapati, M. Späth, L. Knecht, M. Selzer, and B. Nestler.

This document is the Accepted Manuscript version of a Published Work that appeared in final form in Crystal Growth & Design (copyright © 2021 The Authors. Published by American Chemical Society), after peer review and technical editing by the publisher. To access the final edited and published work see https://doi.org/10.1021/acs.cgd.0c01715.

Accepted for publication in Crystal Growth & Design on Apr 21, 2021.

© 2022. This manuscript version is made available under the CC-BY-NC-ND 4.0 license https://creativecommons.org/licenses/by-nc-nd/4.0/

Quantitative phase-field modeling of faceted crystal dissolution processes

Nishant Prajapati,[*,†,¶] Michael Späth,[†,¶] Linus Knecht,[†] Michael Selzer,[†,‡] and Britta Nestler[†,‡]

†*Institute for Applied Materials (IAM-CMS), Karlsruhe Institute of Technology (KIT), Strasse am Forum 7, 76131 Karlsruhe, Germany*

‡*Institute for Digital Materials Science (IDM), Karlsruhe University of Applied Science, Moltkestrasse 30, D-76133 Karlsruhe, Germany*

¶*Authors contributed equally to this work*

E-mail: nishant.prajapati@kit.edu

Abstract

Present article showcases a systematic and generalized phase-field modeling approach for addressing the phenomenon of faceted crystal dissolution in different crystalline solids, in two and three dimensions. A thermodynamically consistent phase-field model was adapted to account for anisotropies in the surface energy and kinetic mobility associated with the crystal surface that evolves during dissolution. Two significant and novel aspects of this work are: (I) the proposed general prescription of anisotropy parameters and (II) quantitative process simulation, within the phase-field modeling framework. The prescription allows to simulate dissolution in different crystal-liquid systems, where the crystal may exhibit arbitrary growth and dissolution facets. Moreover, the order of precedence and relative velocities of facets can be precisely controlled. To demonstrate the procedure of quantitative modeling, we considered the system of α-

quartz in silica-undersaturated solution at the physical conditions from previous experiments, and determined other input model parameters from existing literature. Further, the missing anisotropy parameters were retrieved based on simulations of dissolving single crystals. Following the proposed prescription and the procedure of parameter-set generation, dissolution processes in other crystal-liquid systems at different physical conditions can be modeled. The general applicability, capabilities and performance of this model in capturing diverse system-specific dissolution behavior is demonstrated through representative numerical examples.

Keywords

faceted crystal dissolution, quantitative phase-field modeling, quartz dissolution

1 Introduction

Crystals have always fascinated the mankind, owing to their clarity, long-range order and near perfect symmetry. The processes that lead to their formation and alteration have been the topics of deep scientific interest. In our day-to-day lives, the phenomenon of *crystal growth* can be encountered in the form of ice in a refrigerator, or sugar crystals appearing in a jar of honey. The reverse process, i.e. *crystal dissolution*, is as common as growth, and can be observed in activities as simple as stirring a spoon of salt crystals in a glass of water. In nature, these processes may occur at much longer time scales, for instance, the formation of crystalline minerals such as quartz, granite and calcite, among several others. In geological systems where rocks (e.g. sandstones) are exposed to aqueous undersaturated fluids, provided the physical conditions (i.e. pressure, temperature, fluid composition, etc.) are suitable, dissolution of minerals (e.g. quartz) occurs.[1] Dissolution alters the physical properties of rocks such as porosity,[2] permeability,[3] mechanical strength,[4] among others. Thus, a deep understanding of this phenomenon is imperative for geoscientists and petro-

physicists. Other than this, a wide range of engineering applications of dissolution can also be found in diverse scientific and commercial fields such as geochemistry (e.g. nuclear waste management,[5] geothermal heat recovery[6]), industrial manufacturing (e.g. etching of semiconductors[7]), pharmaceutical[8,9] and food industries,[10] among several others.

At atomistic scale, during dissolution the atoms lying on the crystal surface are released into the solution, due to breakage of atomic bonds. At higher length scales (i.e. microscopic to macroscopic), this leads to reduction in crystal size, accompanied by shape evolution according to the crystal habit. Although the morphologies of the dissolving crystals are known to have no steady-state, it has been shown that a dissolving crystal can attain a steady-state shape under certain conditions.[11] Lacmann et al.[12] theoretically suggested that faces in the dissolution shape are derived by cutting off the corners of the equilibrium form. For mineralogical crystals, Moore[13] stated that faces in the growth shape transform to vertices in the dissolution shape, and vertices in growth become faces in dissolution. In contrast to the crystal growth, where the steady-state faceted morphology, or so-called *growth form* (terminology adopted from Heimann[14]), is determined by the slowly moving faces;[15,16] during the reverse process, the steady-state shape, or so-called *dissolution form* (terminology from Heimann[14]) is dominated by the faster moving facets.[17] Similar inferences were also derived in the early experiments of Heimann,[14] who investigated the dissolution of β-quartz, and deduced that the dissolution forms were bounded by faces with the fastest shift velocities.

In general, crystals can show varying growth and dissolution rates in different crystallographic directions. The occurrence and relative velocities of different facets can be described on the basis of the *Periodic bond chain* (PBC) theory.[18–20] According to this theory, crystal faces can be categorized into three different classes based on the number of so-called *PBC vectors* which are coplanar with the faces. These vectors are measures of the effective zone direction of the periodic patterns in a crystal, and give clues to the understanding of their

morphological development.[18] The three classes of crystal faces are: F (or *flat faces*) containing two or more PBC vectors, S (or *stepped faces*) with one, and K (or *kinked faces*) with no PBC vector. For a representative cubic portion of a crystal lattice bounded by six F-faces, there are twelve S-faces at the cube edges (i.e. intersection of two F-faces), while eight K-faces occur at the corners (i.e. intersection of three F-faces). As the number of PBC vectors increases, the difficulty in removing an atom from the crystal surface also increases. Therefore, the velocities of F-faces are lower than those of S-faces, and K-faces are the fastest moving surfaces.[18] This order of rates is also consistent with the work of Hurst,[21] who constructed a hierarchy of surface characteristics (e.g. different index faces, face edges and corners) for quartz grains, in the ascending order of their dissolution velocities (see Table 1 in the above citation).

In different crystalline materials including organic and inorganic crystals, distinct faces may appear and dissolve at unequal rates, depending upon various process parameters such as chemical composition of the fluid (e.g. different melts,[14] pH,[22] dissolved metal ions[23]), dominant mechanisms (e.g. surface disintegration, bulk diffusion) and their dependencies on physical conditions (e.g. temperature, fluid-flow rate).[24] For instance, the experimental results of dissolution of β-succinic acid (an organic crystalline compound used in pharmaceutical and food industry) report that it dissolves such that S-faces appear at the edges of its growth form.[25] Whereas, for β-quartz (a crystalline silica polymorph which is stable above 573 ^{o}C[26]), dissolution experiments of single crystal spheres in various acid alkali fluoride melts indicate that both S- and K-faces may appear depending upon the melt (see Fig. 9 in Heimann[14]). Similarly, there exists a wide variety of growth and dissolution forms for α-quartz (silica polymorph, stable below 573 ^{o}C).[27] Owing to the thermodynamic stability under ambient conditions, α-quartz is one of the most common minerals in the upper crust and surface of earth.[28,29] Therefore, dissolution of α-quartz has been a topic of intensive experimental research for a long time.[21,30–46] The preceding works studied the influ-

ence of different factors on the kinetics of silica dissolution e.g. temperature,[30,37] saturation state,[39,44,45] molal concentration and presence of cations/salt effect,[34,36,40–42,45] pH,[41] particle size[43] and crystal defects.[33] While most of these works studied the overall kinetics, the facet-specific dissolution rates for α-quartz were also analysed by few of them.[21,31,32,36,39,40,46] It has been found that the basal plane (or so-called c-face) of α-quartz has the fastest shift velocities during dissolution.[32,46] Moreover, over a wide range of experimental conditions, the velocity of the rhombohedral faces has been observed to be higher than the prismatic ones.[36,39] This order of facet velocities is also consistent with those measured by Ostapenko and Mitsyuk[46] in their hydrothermal experiments.

It is evident that experiments have played an important role in understanding the dissolution tendencies of different crystalline materials. However, many a times, they can be arduous to perform or economically less feasible, especially when a series of tests is required for understanding the impact of different process controls. As a viable alternative, computational approaches are powerful tools to derive valuable insights which are otherwise not readily available. Various numerical approaches have been utilized to study the dissolution processes in different minerals, for instance, *Metadynamics* simulations in barite[47] or *Monte Carlo* method for quartz[48] and feldspar.[49] The above two approaches are applicable and limited to atomistic length scales owing to the restrictions of computational costs. Other numerical techniques that are well-suited at microscopic and higher length scales include e.g. the *Level-set* method[50] for simulating crystal precipitation and dissolution in porous media,[51,52] or *ab initio* mechanistic modeling of the dissolving succinic acid crystals.[17,53] Another methodology known as the *Dynamic mesh* approach with surface relaxation has also been used to model dissolution and investigate the process controls such as presence of metal ions in calcite crystals.[23] For a detailed comparative analysis of several other simulation methods for mineral dissolution, also including the advective flow, interested readers are referred to the recent review article of Molins et al..[54]

In the last decade, a diffuse interface approach, known as *phase-field* method/model (PFM), has emerged as a powerful computational tool for modeling mineral precipitation processes in rocks.[55–64] Long-established in the materials science community (see review articles[65–68]), the PFM enables an efficient treatment of the interface motion due to complex topological changes that occur during microstructural processes such as phase-transitions[69,70] and other moving boundary problems like crack propagation,[71] multiphase-flow,[72] among others. Moreover, the PFM has also been utilized to simulate mineral dissolution processes in one (1-D)[73] and two dimensions (2-D).[74,75] However, none of these works accounted for anisotropies in their modeling, which is indispensable for addressing the phenomenon of faceted crystal dissolution. In this work, we present a generalized anisotropic PFM, well-suited for simulating faceted crystal dissolution processes in arbitrary crystal systems. In order to showcase the model's general applicability as well as capabilities, in addition to a case of 2-D crystal, several representative examples of dissolving crystals in 3-D are also illustrated.

The present article is organized as follows. Section 2 elaborates the methods utilized for this study. They include I) equations of the employed PFM, II) its adaptation for simulating faceted crystal dissolution, and III) procedure to generate the complete parameter set for a given crystal system at the considered physical conditions. In section 3, we present the simulation results pertaining to dissolution of single crystals for different materials. This includes the representative model validation cases I) in 2-D for elucidating the novel anisotropy adaptation, followed by II) 3-D examples of two different crystal-liquid systems. Further, we demonstrate the approach to quantitatively model the dissolution process using the adapted PFM by considering the system of α-quartz crystals dissolving in silica-undersaturated water at the experimental conditions given in previous literature. Finally, we conclude the article in section 4 by recapitulating the main inferences drawn from the present work and directions

for future investigations.

2 Methods

In section 2.1, the equations of a generalized phase-field model for dissolution are discussed. The model adaptation in the context of simulating faceted crystal dissolution is elucidated in section 2.2. Section 2.3 elaborates the procedure utilized to determine the complete phase-field parameter set at the given physical conditions (of pressure p, temperature T, and concentration $\mathfrak{c}$), required for the quantitative modeling of the process. Exemplarily, we considered the dissolution of α-quartz in silica-undersaturated water, as all the required process parameters were readily available from the literature. This procedure can be utilized to determine the complete parameter set for other crystal-liquid systems at different physical conditions. All the parameters along with their symbols are listed in table A9.

2.1 Phase-field model for dissolution

In a physical domain Ω containing a solid s and a liquid l phase, we consider a duplet $\boldsymbol{\phi}(\boldsymbol{x},t) = [\phi_s(\boldsymbol{x},t),\ \phi_l(\boldsymbol{x},t)]$ of phase-fields. Each phase-field $\phi_\alpha : \Omega \times \mathbb{R}_0^+ \to [0,1]$ describes the presence of phase $\alpha \in \{s,l\}$ at the spatial point $\boldsymbol{x} \in \Omega$ and time $t \in \mathbb{R}_0^+$. At each spatial point, the summation constraint $\phi_s(\boldsymbol{x},t) + \phi_l(\boldsymbol{x},t) = 1$ is satisfied. The region completely occupied by a single phase α is known as α-*bulk*, mathematically defined as $\mathcal{B}_\alpha = \{\boldsymbol{x} \in \Omega \mid \phi_\alpha(\boldsymbol{x},t) = 1\}$. The total *bulk* region is given by $\mathcal{B} = \mathcal{B}_s \cup \mathcal{B}_l$, as the union of solid-*bulk* $\mathcal{B}_s$ and liquid-*bulk* $\mathcal{B}_l$. The interface between the solid and liquid phases is described by a diffuse region of a finite width, and is defined as $\mathcal{I}_{sl} = \{\boldsymbol{x} \in \Omega \backslash \mathcal{B} \mid \phi_s(\boldsymbol{x},t) + \phi_l(\boldsymbol{x},t) = 1\}$. The *Helmholtz free energy* $\mathcal{F}$ of this system is formulated as the sum of bulk $\mathcal{F}_{\text{bulk}}$ and interface $\mathcal{F}_{\text{interface}}$ free energy contributions

$$\mathcal{F}(\boldsymbol{\phi}, \boldsymbol{\nabla\phi}) = \mathcal{F}_{\text{bulk}} + \mathcal{F}_{\text{interface}} = \int_\Omega \{\mathfrak{f}_{\text{bulk}}(\boldsymbol{\phi}) + \mathfrak{f}_{\text{interface}}(\boldsymbol{\phi}, \boldsymbol{\nabla\phi})\}\, \mathrm{d}\Omega, \tag{1}$$

where $\mathfrak{f}_{\text{bulk}}(\boldsymbol{\phi})$ and $\mathfrak{f}_{\text{interface}}(\boldsymbol{\phi}, \boldsymbol{\nabla\phi})$ are the bulk and interface free energy density, respectively. The *bulk free energy density* is given by

$$\mathfrak{f}_{\text{bulk}}(\boldsymbol{\phi}) = \mathfrak{f}_s\phi_s + \mathfrak{f}_l\phi_l \tag{2}$$

as a linear volumetric interpolation of the bulk-free energy densities $\mathfrak{f}_s$ and $\mathfrak{f}_l$ of the solid and liquid phase, respectively. In the present work, the solid phase is assigned a free energy density of $\mathfrak{f}_s = 0$ and a non-zero free energy density $\mathfrak{f}_l \neq 0$ is chosen for the liquid phase. The driving force for the dissolution process arises from the difference of the solid and liquid free energy densities $\Delta f_{sl}^{\text{Diss}} = \mathfrak{f}_l - \mathfrak{f}_s$. The interface free energy density is formulated as

$$\mathfrak{f}_{\text{interface}}(\boldsymbol{\phi}) = \varepsilon a(\boldsymbol{\phi}, \boldsymbol{\nabla\phi}) + \frac{1}{\varepsilon}\omega(\boldsymbol{\phi}) \tag{3}$$

as the sum of potential- and gradient energy density, $\omega(\boldsymbol{\phi})/\varepsilon$ and $\varepsilon a(\boldsymbol{\phi}, \boldsymbol{\nabla\phi})$, respectively. The scalar length scale parameter ε controls the width of diffuse interface. A *double-obstacle potential energy density* of the following form

$$\frac{1}{\varepsilon}\omega(\boldsymbol{\phi}) = \begin{cases} \frac{16}{\varepsilon\pi^2}\gamma_{sl}\phi_s\phi_l & \text{if } \boldsymbol{\phi} \in \{\boldsymbol{\phi} \mid \phi_s + \phi_l = 1, \text{ and } \phi_s, \phi_l \geq 0\} \\ \infty & \text{else,} \end{cases} \tag{4}$$

is chosen, where γ_{sl} represents the surface energy of solid-liquid interface. The choice of the double-obstacle potential results in a finite width of the diffuse interface. From the computational point of view, the advantage of this choice lies in the fact that the phase-field evolution equations (see eq. (6) and (7)) need to be solved and updated only in the diffuse interface region and not in the complete simulation domain[76]. The *gradient energy density* serves as an energetic penalty due to the presence of diffuse interface region, and is

formulated as

$$\varepsilon a(\boldsymbol{\phi}, \boldsymbol{\nabla\phi}) = \varepsilon\gamma_{sl}\{a_{sl}^{\mathrm{cap}}(\mathfrak{n}_{sl})\}^2|\mathfrak{q}_{sl}|^2, \tag{5}$$

where $\mathfrak{q}_{sl} = \phi_s\boldsymbol{\nabla}\phi_l - \phi_l\boldsymbol{\nabla}\phi_s$ is the phase-field gradient vector oriented perpendicular to the solid-liquid interface, and $\mathfrak{n}_{sl} = \mathfrak{q}_{sl}/|\mathfrak{q}_{sl}|$ is the unit vector pointing in the same direction. The scalar-valued capillary function $a_{sl}^{\mathrm{cap}}(\mathfrak{n}_{sl})$ accounts for anisotropy in the surface energy of the solid-liquid interface. The form of the capillary anisotropy function and the prescription of input parameters in the context of modeling faceted crystal dissolution are discussed in section 2.2. The evolution of solid and liquid phase-fields is formulated as[77]

$$\frac{\partial\phi_s}{\partial t} = -\frac{\mu_{sl}(\mathfrak{n}_{sl})}{2\varepsilon}\left\{\frac{\delta\mathcal{F}_{\mathrm{interface}}}{\delta\phi_s} - \frac{\delta\mathcal{F}_{\mathrm{interface}}}{\delta\phi_l} - \frac{8\sqrt{\phi_s\phi_l}}{\pi}\left(\frac{\delta\mathcal{F}_{\mathrm{bulk}}}{\delta\phi_l} - \frac{\delta\mathcal{F}_{\mathrm{bulk}}}{\delta\phi_s}\right)\right\}, \tag{6}$$

$$\frac{\partial\phi_l}{\partial t} = -\frac{\mu_{sl}(\mathfrak{n}_{sl})}{2\varepsilon}\left\{\frac{\delta\mathcal{F}_{\mathrm{interface}}}{\delta\phi_l} - \frac{\delta\mathcal{F}_{\mathrm{interface}}}{\delta\phi_s} - \frac{8\sqrt{\phi_s\phi_l}}{\pi}\left(\frac{\delta\mathcal{F}_{\mathrm{bulk}}}{\delta\phi_s} - \frac{\delta\mathcal{F}_{\mathrm{bulk}}}{\delta\phi_l}\right)\right\}, \tag{7}$$

such that a monotonic decrease in the free energy of the system with time is ensured. The term $8\sqrt{\phi_s\phi_l}/\pi$ ensures the correct interface kinetics with the utilized double-obstacle potential in eq. (4).[77,78] The difference of the variational derivatives of the bulk free energy yields the dissolution driving force, i.e. $\delta\mathcal{F}_{\mathrm{bulk}}/\delta\phi_s - \delta\mathcal{F}_{\mathrm{bulk}}/\delta\phi_l = f_l - f_s = \Delta f_{sl}^{\mathrm{Diss}}$. The prefactor $\mu_{sl}(\mathfrak{n}_{sl})$ represents the kinetic mobility of the solid-liquid interface, formulated as

$$\mu_{sl}(\mathfrak{n}_{sl}) = \mu_{sl}^0 a_{sl}^{\mathrm{kin}}(\mathfrak{n}_{sl}), \tag{8}$$

where μ_{sl}^0 denotes the kinetic mobility coefficient of the solid-liquid interface, and $a_{sl}^{\mathrm{kin}}(\mathfrak{n}_{sl})$ is a scalar valued anisotropy function accounting for the direction-dependent particle detachment kinetics. In the context of faceted crystal dissolution, the chosen form of the kinetic anisotropy function and the prescription of input parameters are discussed in section 2.2. The model equations are implemented in a parallel multi-physics computational framework known as PACE3D (v.2.5.1),[79,80] in the C programming language. It is noteworthy that,

in the present phase-field model, due to the incorporation of anisotropies, the derivation of analytical sharp interface relations is not straight-forward and is an open problem in the phase-field community.

2.2 Modeling faceted crystal dissolution within phase-field framework

Based on the growth habit, a crystal develops its faceted *growth form* bounded by the slowly moving facets.[15,16] We refer to the facets present in the growth form as *growth facets*. During dissolution, different faces may appear at the edges and/or corners of the growth form depending upon the crystal habit, and dissolve at different velocities. We refer to these faces as *dissolution facets*. The final *dissolution form* is bounded by the fast moving dissolution facets[17] (as also comprehensively discussed in section 1). In order to incorporate these tendencies in the phase-field model, we chose a capillary anisotropy function of the following form

$$a_{sl}^{\mathrm{cap}}(\mathfrak{n}_{sl}) = \max_k \left\{ \mathfrak{n}_{sl} \cdot \boldsymbol{\eta}_k^{\mathrm{cap}} \right\}, \qquad (k = 1, \ldots, n_{\mathrm{cap}}), \tag{9}$$

where the scalar function $\max_k$ returns the largest argument in the braces, the operator $(\cdot)$ denotes the scalar (or dot) product of two vectors, and $\mathfrak{n}_{sl}$ represents the unit phase-field gradient vector. $\boldsymbol{\eta}_k^{\mathrm{cap}}$ denotes k^{th} element of the set $\boldsymbol{\mathcal{N}}^{\mathrm{cap}} = \{\boldsymbol{\eta}_1^{\mathrm{cap}}, \ldots, \boldsymbol{\eta}_{n_{\mathrm{cap}}}^{\mathrm{cap}}\}$ of n_{cap} geometric vectors that should be appropriately chosen based on crystal system (please refer to subsection 2.2.1). The capillary anisotropy is responsible for the shape attained by a crystal under vanishing driving forces due to surface energy minimization. It is noteworthy that for any input set of vertex vectors corresponding to a convex faceted crystal, the chosen form of capillary anisotropy function (eq. (9)) ensures that the surface stiffness never becomes negative. Alternatively, the Frank plot (i.e. polar plot of 1/surface energy) is always non-concave. Hence, a regularization of equations (6) and (7) to avoid an ill-posed evolution

equation is not required, and is not included in the present model. Further, in order to control the appearance and relative rates of different growth as well as dissolution facets during the crystal dissolution process, we chose a kinetic anisotropy function of the following form[58]

$$a_{sl}^{\mathrm{kin}}(\mathfrak{n}_{sl}) = \left[1 + \delta\left(\max_k\left\{\mathfrak{n}_{sl}\cdot\boldsymbol{\eta}_k^{\mathrm{kin}}\right\} - \max_{k-1}\left\{\mathfrak{n}_{sl}\cdot\boldsymbol{\eta}_k^{\mathrm{kin}}\right\}\right)\right]\cdot\max_k\left\{\mathfrak{n}_{sl}\cdot\boldsymbol{\eta}_k^{\mathrm{kin}}\right\}, \quad (k=1,\ldots,n_{\mathrm{kin}}), \tag{10}$$

where the function $\max_{k-1}$ returns the second largest value in the braces, δ denotes the anisotropy strength parameter and $\boldsymbol{\eta}_k^{\mathrm{kin}}$ represents k^{th} element of the set $\boldsymbol{\mathcal{N}}^{\mathrm{kin}} = \{\boldsymbol{\eta}_1^{\mathrm{kin}},\ldots,\boldsymbol{\eta}_{n_{\mathrm{kin}}}^{\mathrm{kin}}\}$ of n_{kin} geometric vectors to be appropriately chosen based on the crystal system, as elaborated in the forthcoming sub-section 2.2.1.

2.2.1 Prescription of anisotropy parameters

In the context of phase-field modeling of faceted crystal dissolution, we propose a generalized procedure to prescribe the input set of geometric parameters for the capillary and kinetic anisotropy functions. Here we remark that, although the forms of anisotropy functions have been taken from previous literature, the general prescription of input anisotropy parameters discussed in the following part of this section is novel and has never been used before. For the purpose of illustration, we consider a hypothetical crystal system with hexagonal growth and dissolution forms, as shown in figure 1a. The prescription of input parameters for the two functions is as follows:

- **For capillary anisotropy function:** We chose $\boldsymbol{\mathcal{N}}^{\mathrm{cap}}$ as the set of vertex vectors of the dissolution form, see figure 1b. The resulting polar plot of the surface energy for the considered hexagonal crystal system is schematically illustrated in the same figure. Here, the directions of local minima correspond to those of the normal vectors of different dissolution facets. As a result, these facets are ought to be energetically favorable, and are expected to stay during late stages of dissolution. The corresponding

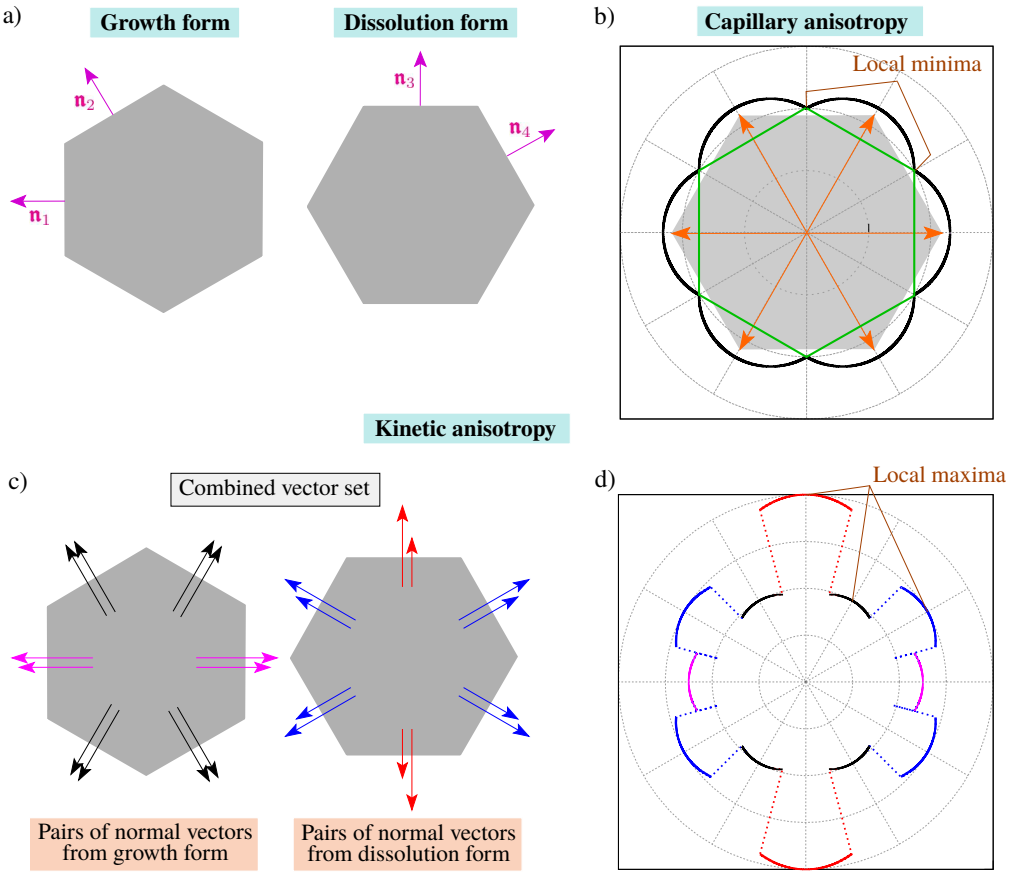

Figure 1: Prescription of anisotropy parameters. a) An exemplary crystal with the given hexagonal growth and dissolution forms. b) Schematics illustrating the set of input vectors (i.e. vertex vectors of dissolution form in orange color) for the capillary anisotropy function and the corresponding polar surface energy plot (in black) and Frank plot (in green). The facet energies are given by values at the local minima in different directions. c) Schematics illustrating the combined set of pairs of facet normal vectors of the growth and dissolution forms as input for the kinetic anisotropy function, and d) the corresponding polar plot of kinetic mobility. The dotted parts in the plot represent jumps in kinetic mobility. The color of different parts of the polar mobility plot corresponds to the vector pairs controlling the mobilities in the respective directions. The vector pairs of facets belonging to same family are depicted in same color. The facet mobilities are given by values at the local maxima in different directions.

Frank plot (for the case of unit surface energy for all six facets) is shown in green colored lines in figure 1b. This plot is non-concave in nature, thereby implying a non-negative surface stiffness.

- **For kinetic anisotropy function:** We chose $\mathcal{N}^{\text{kin}}$ as the set of pairs of input vectors parallel to the normal vectors (see figure 1a) of all the growth and dissolution facets,

as schematically illustrated in figure 1c. In general, the vectors of each vector pair (in the set $\boldsymbol{\mathcal{N}}^{\text{kin}}$) corresponding to a facet $f \in \{1, \ldots, \hat{F}\}$ and parallel to the facet normal $\mathbf{n}_f$, differ in magnitude through the facet-specific anisotropy strength parameters $\mathcal{A}_f \in [0, 1]$. Thus, the set containing all the facet-specific anisotropy strength parameters is represented as $\hat{\boldsymbol{\mathcal{A}}} = \{\mathcal{A}_1, \ldots, \mathcal{A}_f, \ldots, \mathcal{A}_{\hat{F}}\}$, where $\hat{F}$ denotes the total number of facets appearing during the crystal dissolution process. After appropriately setting the value of anisotropy strength parameter δ, each $\mathcal{A}_f$ should be chosen to obtain the desired kinetic mobility of the corresponding facet f, as schematically illustrated by the polar plot of kinetic mobility in figure 1d for the considered hexagonal crystal system. The kinetic mobilities of different facets are given by values at the local maxima present in the directions corresponding to their normals. Increasing the difference of magnitude between a vector pair (by decreasing $\mathcal{A}_f$) increases the mobility in the direction pointed by the pair. When multiple facets correspond to the same crystallographic facet family and are assigned with the same anisotropy strength parameter $\mathcal{A}_f$ (e.g. c, r, m-facets in α-quartz), we define a new reduced set $\boldsymbol{\mathcal{A}}$ which contains only the strength parameters of different facet families. By appropriate calibration of the anisotropy parameters (i.e. $\boldsymbol{\mathcal{A}}$ and δ), the order of precedence and relative velocities of different facets can be controlled. It is noteworthy that, during dissolution, if a crystal system exhibits additional intermediate facets which are not present in the growth and dissolution forms, these facets should be appropriately accounted in the sets $\boldsymbol{\mathcal{N}}^{\text{kin}}$ and $\boldsymbol{\mathcal{A}}$.

2.3 Physical parameters for α-quartz dissolution

In this section, we elaborate the method adopted to determine the physical parameters for α-quartz dissolution. For the present work, the pressure $p = 1$ atm and temperature $T = 166^{\text{o}}$ C, corresponding to one of the experimental conditions of Gratz and Bird,[39] were chosen for the following reasons: I) for the purpose of model validation, the quantitative information about the facet velocities is available in their work, and II) it was possible to determine

the complete set of phase-field parameters at their physical $(p, \mathfrak{c}, T)$ conditions from the existing literature. The procedure to determine the complete parameter set is elucidated in the following sub-sections. The set is also listed in column 4 of table 4. For the sake of convenience, the phase-field model parameters associated with the binary interface of the α-quartz–water system are represented with the subscript qw, q and w being α-quartz and water, respectively. For other solid-liquid systems considered in this work, the subscript sl is retained.

2.3.1 Surface energy of interface

We chose the surface energy of the quartz-water interface of $\gamma_{\mathrm{qw}} = 0.36$ J/m^2 given in Parks.[81]

2.3.2 Driving force of dissolution

Quartz crystal growth and dissolution is governed by the silica-water chemical reaction, which reads

$$\mathrm{SiO_2(s)} + 2\mathrm{H_2O(l)} \rightleftharpoons \mathrm{H_4SiO_4(aq)}, \tag{11}$$

where (s), (l) and (aq) denote the solid, liquid and aqueous phases, respectively. The change in molar Gibbs free energy ΔG of the reaction is given by

$$\Delta G = RT \ln \mathcal{S}, \tag{12}$$

where R denotes the gas constant and $\mathcal{S}$ represents the saturation index of the fluid. For dilute solutions (i.e. fulfilling the ideal solution assumptions), the saturation index is well-

approximated as

$$\mathcal{S} = \frac{\mathfrak{c}_{\mathrm{H_4SiO_4}}}{\mathfrak{c}^{\mathrm{eq}}_{\mathrm{H_4SiO_4}}} \tag{13}$$

in terms of $\mathfrak{c}_{\mathrm{H_4SiO_4}}$ and $\mathfrak{c}^{\mathrm{eq}}_{\mathrm{H_4SiO_4}}$, the actual and equilibrium concentration of orthosilicic acid (H_4SiO_4), respectively. Deviation of actual concentration from the equilibrium value generates a driving force for precipitation (when $\mathcal{S} > 1$) or dissolution (when $\mathcal{S} < 1$). Following the work of Wendler et al.,[58] the driving force of dissolution ($\Delta f^{\mathrm{Diss}}_{\mathrm{qw}}$) for the quartz-water system, that enters the phase-field model, can be mathematically expressed as

$$\Delta f^{\mathrm{Diss}}_{\mathrm{qw}} = (\mathfrak{c}^{\mathrm{eq}}_{\mathrm{H_4SiO_4}} - \mathfrak{c}_{\mathrm{H_4SiO_4}}) \frac{\Delta \mathcal{F}}{V^{\mathrm{H_2O}}_{\mathrm{m}}}, \tag{14}$$

where $\Delta\mathcal{F}$ is the change in the Helmholtz free energy of the system, and $V^{\mathrm{H_2O}}_{\mathrm{m}}$ is the molar volume of water. Using the thermodynamic relation $\Delta\mathcal{F} = \Delta G - p\Delta V$ along with eqs. (12) (13) and (14) yields

$$\Delta f^{\mathrm{Diss}}_{\mathrm{qw}} = \mathfrak{c}^{\mathrm{eq}}_{\mathrm{H_4SiO_4}} \frac{(1-\mathcal{S})(RT\ln\mathcal{S} - p\Delta V)}{V^{\mathrm{H_2O}}_{\mathrm{m}}}, \tag{15}$$

where ΔV is the difference between the molar volumes of quartz and water. In the experiments of Gratz and Bird,[39] the actual and equilibrium concentrations of orthosilicic acid were $\mathfrak{c}_{\mathrm{H_4SiO_4}} = 193$ ppm and $\mathfrak{c}^{\mathrm{eq}}_{\mathrm{H_4SiO_4}} = 385$ ppm, thereby resulting in a saturation index of $\mathcal{S} = 0.501$. For the above $(p, \mathfrak{c}, T)$ conditions, a driving force of $\Delta f^{\mathrm{Diss}}_{\mathrm{qw}} = -26881$ J/m^3 is obtained.

2.3.3 Kinetic mobility of interface

The velocity v_{qw} of quartz-water interface during dissolution is given by[30]

$$v_{\mathrm{qw}} = V^{\mathrm{qtz}}_{\mathrm{m}} k_+ (1-\mathcal{S}), \tag{16}$$

where $V_{\mathrm{m}}^{\mathrm{qtz}}$ and k_+ denote the molar volume of quartz and the dissolution rate constant, respectively. We chose a value of $k_+ = 2.09 \times 10^{-6}$ s^{-1} (or $\log k_+ = -5.68$) corresponding to the temperature of 162°C from Worley et al.,[41] as it is the best available estimate close to the temperature considered in the present work (i.e. 166°C). For a flat interface, the kinetic mobility is given by

$$\mu_{\mathrm{qw}}^{0} = \frac{v_{\mathrm{qw}}}{\Delta f_{\mathrm{qw}}^{\mathrm{Diss}}} = \frac{V_{\mathrm{m}}^{\mathrm{qtz}} V_{\mathrm{m}}^{\mathrm{H_2O}} k_+}{\mathfrak{c}_{\mathrm{H_4SiO_4}}^{\mathrm{eq}} RT \ln \mathcal{S}}. \tag{17}$$

which connects the dissolution rate coefficient k_+ with the phase-field evolution equation (6) and (7). With the known values of all the parameters on the right hand side of eq. (17), we obtain an interface mobility of $\mu_{\mathrm{qw}}^{0} = 8.79 \times 10^{-16}$ m^4/J-s.

2.3.4 Anisotropy parameters for α-quartz dissolution

We discuss the procedure to determine the anisotropy parameters of capillary and kinetic anisotropy functions for the dissolution of α-quartz in silica-undersaturated water. For the sake of clarity, we mention that the miller index notation used in this work is such that miller indices with parentheses represent a specific plane and those with braces represent a family of planes. Based on the dissolution experiments of single crystal spheres of β-quartz in different melts, Heimann[14] proposed the dissolution forms for different growth forms. In particular, the Type A growth form corresponds to the hexagonal dipyramid geometry, see figure 2a. Such hexagonal growth habit is also exhibited by certain twinned α-quartz crystals, when the growth rates of rhombohedral r $(01\bar{1}1)$ and z $(1\bar{1}01)$ facets do not differ, thereby leading to indistinguishable rhombohedral facets.[27,82] In the absence of precise dissolution form of α-quartz in literature, for the present work, we chose the hexagonal-dipyramid growth form with m $\{10\bar{1}0\}$ and r $\{10\bar{1}1\}$ & $\{10\bar{1}\bar{1}\}$ facets for α-quartz, and adopt the dissolution form with c (0001), $(000\bar{1})$ and $\{11\bar{2}2\}$, $\{11\bar{2}\bar{2}\}$ facets from Heimann[14] (Fig. 9, corresponding to Type A β-quartz), as also shown in figure 2a. For the sake of convenience, we refer to the

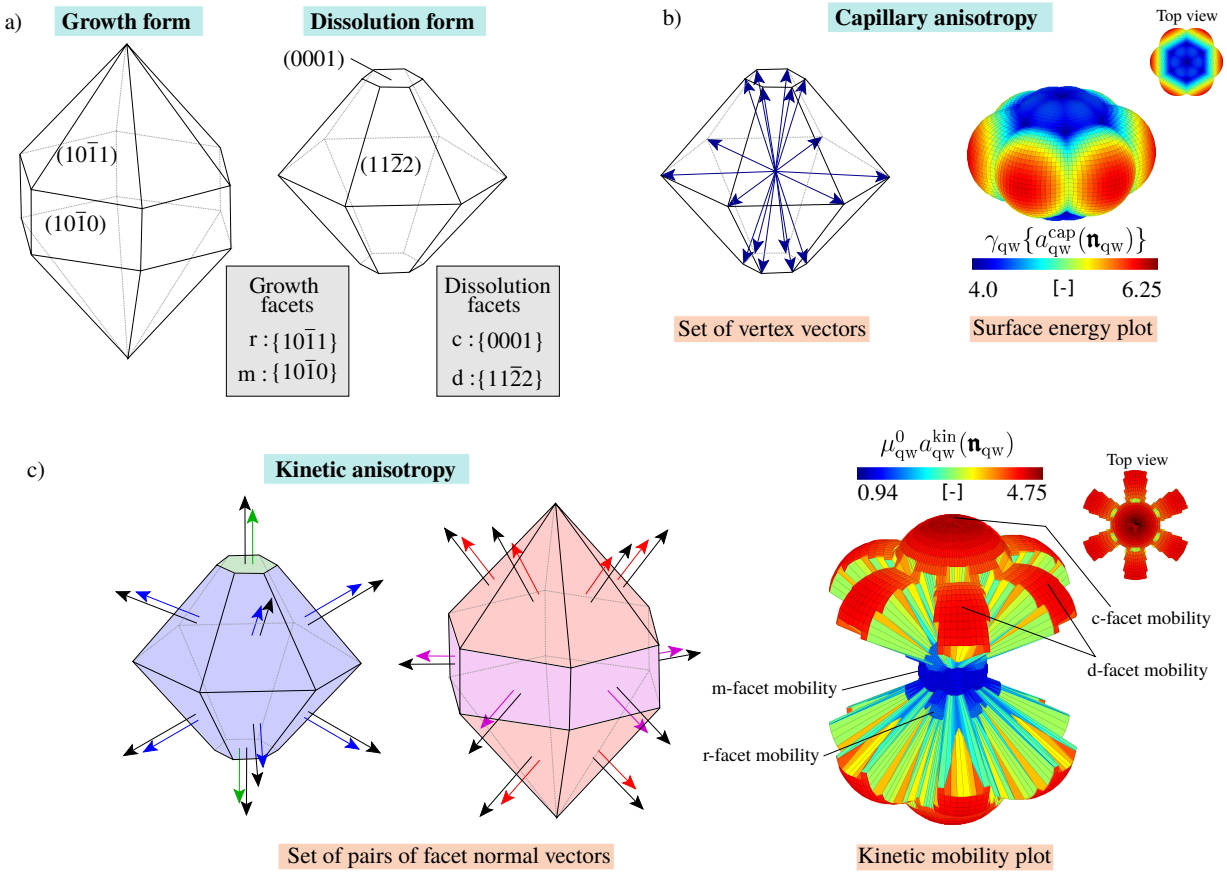

Figure 2: a) Chosen growth and dissolution forms for α-quartz (figure adapted from Heimann[14]). b) Set of vertex vectors of the 3-D dissolution form and the corresponding polar plot of surface energy. c) Combined set of pairs of facet normal vectors of the 3-D growth and dissolution forms, and the corresponding polar plot of the kinetic mobility.

facets with miller indices $\{11\bar{2}2\}$ and $\{11\bar{2}\bar{2}\}$ as d-facets. Following the proposed generalized prescription (discussed in section 2.2.1), we determine the anisotropy parameters for α-quartz as follows:

- **Input parameters for capillary anisotropy function:** For the considered dissolution form of α-quartz (figure 2a), the input set of vertex vectors (illustrated in dark blue color in figure 2b) were chosen such that the surface energy of c- and d-facets are equal, as given in table 5. The resulting polar plot of the surface energy is depicted in figure 2b.

- **Input parameters for kinetic anisotropy function:** The kinetic anisotropy ac-

counts for the relative velocities of different facets. Thus, the parameters need to be calibrated based on the dissolution tendencies of α-quartz. For the basal c-face, Liepmann[32] found the velocity of $v_c/v_m \sim 6$ relative to the m-facet (also mentioned in Gratz and Bird[40]). For the rhombohedral r-facet, the relative rates v_r/v_m in the range of $1.37 - 1.44$ in different alkaline solutions have been reported at the experimental conditions considered in the present work.[39] The order of aforementioned facet velocities is consistent with that reported by Ostapenko and Mitsyuk.[46] For the d-facet, no values of the velocity could be found in literature. Based on the dissolution experiments of single crystals of α-quartz, Hurst[21] proposed that the junctions between edges (i.e. d-facet in α-quartz) and corners (i.e. c-facet in α-quartz) dissolve faster than the low index prism facets (i.e. m-facet in α-quartz). This order is also consistent with the Periodic bond chain (PBC) theory,[18–20] that suggest that *stepped* S (i.e. d-facet in α-quartz) and *kinked* K (i.e. c-facet in α-quartz) faces dissolve at faster rates than *flat* F faces (i.e. m- and r-facets in α-quartz). Moreover, K faces are expected to possess higher velocity than the S faces, as no PBC vector is present along the plane for the former. Thus, we chose the value of $v_d/v_m \sim 4$ for the d-facet.

3 Results and discussions

Through representative model validation examples for different crystal systems using a non-dimensional phase-field parameter set, section 3.1 demonstrates the general applicability and performance of the proposed anisotropy prescription discussed in section 2.2.1. In section 3.2, we showcase a modeling application to quantitatively address the phenomenon of faceted crystal dissolution at real experimental conditions, by exemplarily considering the system of α-quartz in silica-undersaturated water and utilizing the physical parameters determined in section 2.3.

Table 1: Sets of non-dimensional phase-field parameters for the model validation examples

Model parameters	Hexagonal	Type B β-quartz	β-succinic acid
Grid cell size (Δx)	1	1	1
Time step width (Δt)	0.001	0.0008	0.001
Solid-liquid interface energy (γ_{sl})	4.0	4.0	4.0
Length scale parameter (ε)	4	4	4
Kinetic mobility of solid-liquid interface (μ_{sl}^{0})	1.0	1.0	1.0
Driving force for dissolution ($\Delta f_{sl}^{\mathrm{Diss}}$)	-0.15	-0.2999	-0.2999

3.1 Model validation

In section 3.1.1, we elucidate the influence of facet-specific anisotropy strength parameters on the crystal shape evolution through the simulations of dissolution of a two-dimensional (2-D) hexagonal-shaped crystal with the growth and dissolution forms illustrated in figure 1. Sections 3.1.2 and 3.1.3 showcase the model applications in 3-D to real crystal systems of Type B β-quartz (see Heimann[14]) and β-succinic acid (see Snyder et al.[25]), respectively. The set of phase-field parameters for the model validation examples are given in table 1.

3.1.1 Crystal system with hexagonal growth and dissolution forms

We consider a 2-D hexagonal solid crystal dispersed in liquid as depicted in figure 3a, such that the crystal exhibits the growth and dissolution forms shown in figure 1a. In the diffuse interface description (in figure 3b), the phase-field variable ϕ_s determines the presence of crystal (where $\phi_s = 1$), liquid (where $\phi_s = 0$) and the interface (where $0 < \phi_s < 1$). The input set of vertex vectors for the capillary anisotropy function from the dissolution form are listed in table A1. Figure 3c depicts the variation of surface energy in different directions. The set of pairs of normal vectors for the kinetic anisotropy function from growth and dissolution forms are given in table A2, where the facet-specific anisotropy strength parameter set $\boldsymbol{\mathcal{A}} = \{\mathcal{A}_1, \mathcal{A}_2, \mathcal{A}_3, \mathcal{A}_4\}$ controls the mobilities of the growth and dissolution facets. The parameters $\mathcal{A}_1$ - $\mathcal{A}_4$ correspond to the facet families with the normal vectors $\mathbf{n}_1$ - $\mathbf{n}_4$, as depicted in figures 1a and 3d,e. Simulations were performed for the following

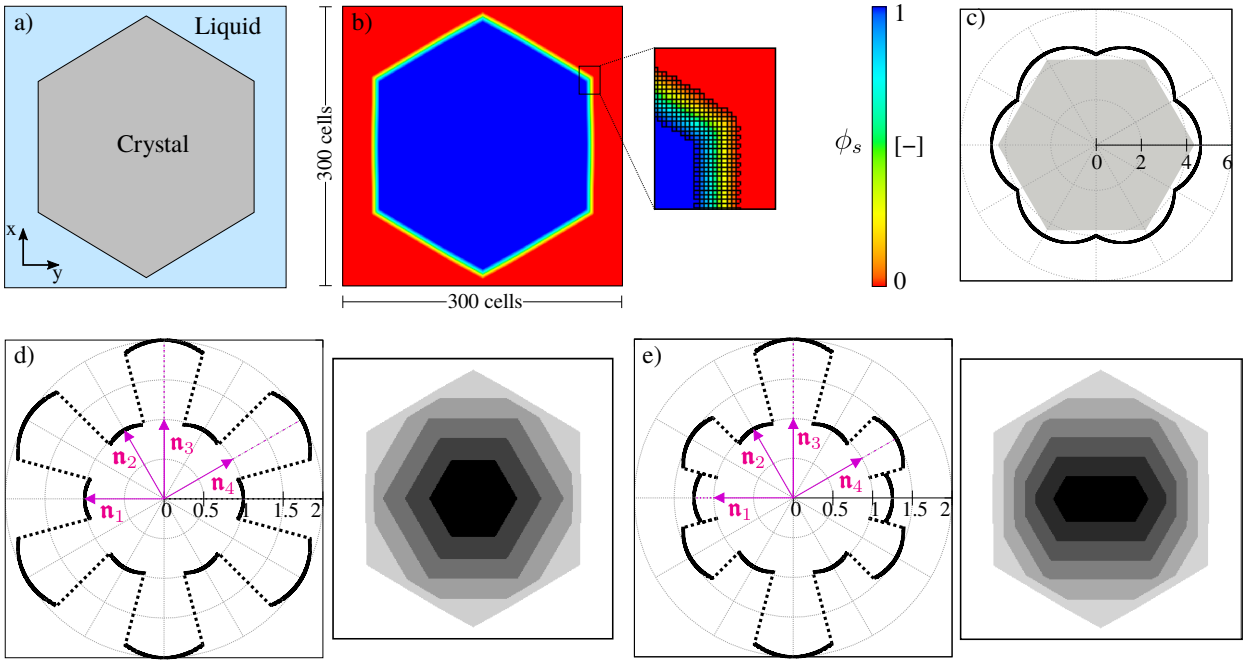

Figure 3: a) Sharp and b) diffuse interface description of a crystal-liquid system, with the crystal exhibiting hexagonal growth and dissolution forms. The phase-field variable ϕ_s varies from 0 to 1 in the diffuse interface as shown in the zoomed inset picture. The interface is resolved by a sufficient number of grid cells. c) Polar plot of the surface energy of the interface for the chosen set of vertex vectors of the dissolution shape (in grey) as input parameters for the capillary anisotropy function. Polar plot of kinetic mobility (left) and the different representative stages of the simulated crystal dissolution (right) for the set of facet-specific anisotropy strength parameters d) $\boldsymbol{\mathcal{A}_1} = \{1.0, 1.0, 0.999, 0.999\}$ and e) $\boldsymbol{\mathcal{A}_2} = \{0.99975, 1.0, 0.999, 0.9995\}$. The dotted parts of the polar plots indicate jumps in the kinetic mobility. These representative stages of crystal dissolution (from light grey to black color) correspond to the shapes attained after every 54,000 non-dimensional simulation time-steps.

two sets of the facet-specific anisotropy strength parameters: $\boldsymbol{\mathcal{A}_1} = \{1.0, 1.0, 0.999, 0.999\}$ and $\boldsymbol{\mathcal{A}_2} = \{0.99975, 1.0, 0.999, 0.9995\}$. The value of anisotropy strength parameter δ in eq. (10) was set to 1000. Set $\boldsymbol{\mathcal{A}_1}$ results in an equal kinetic mobility of the dissolution facets (with normals $\mathbf{n}_3$ and $\mathbf{n}_4$), which is twice the corresponding value for the growth faces (with normals $\mathbf{n}_1$ and $\mathbf{n}_2$), as depicted in the polar plot of the interface mobility in figure 3d (on the left). Different representative stages of the simulated dissolution are shown (on the right) in the same figure in different shades of grey. The initial shape is shown in the lightest shade of grey, and the shapes with darker shades correspond to later times. As expected, the dissolution facets appear at the corners of the intersections of the growth facets. Due to

higher mobility of the dissolution facets, they move at faster rates than the growth facets. Moreover, as the mobility of all the dissolution facets is equal, the subsequent dissolution occurs such that the crystal maintains its shape. For the set $\boldsymbol{\mathcal{A}_2}$, all the facet families have different mobilities, as depicted in the plot in figure 3e. Thus, the facets with higher kinetic mobility dissolve more rapidly and vice versa, as illustrated in figure 3e on the right.

3.1.2 Dissolution of β-quartz

Heimann[14] determined the growth and dissolution forms of different types of β-quartz by analysing a series of experiments of spherical single crystals dissolving in different acid alkali fluoride melts. As an example, we consider the Type B β-quartz (in Heimann[14]) with the growth and dissolution forms as shown in figure 4a. Based on our proposed prescription, the input set of anisotropy vectors for the capillary and kinetic anisotropy functions were

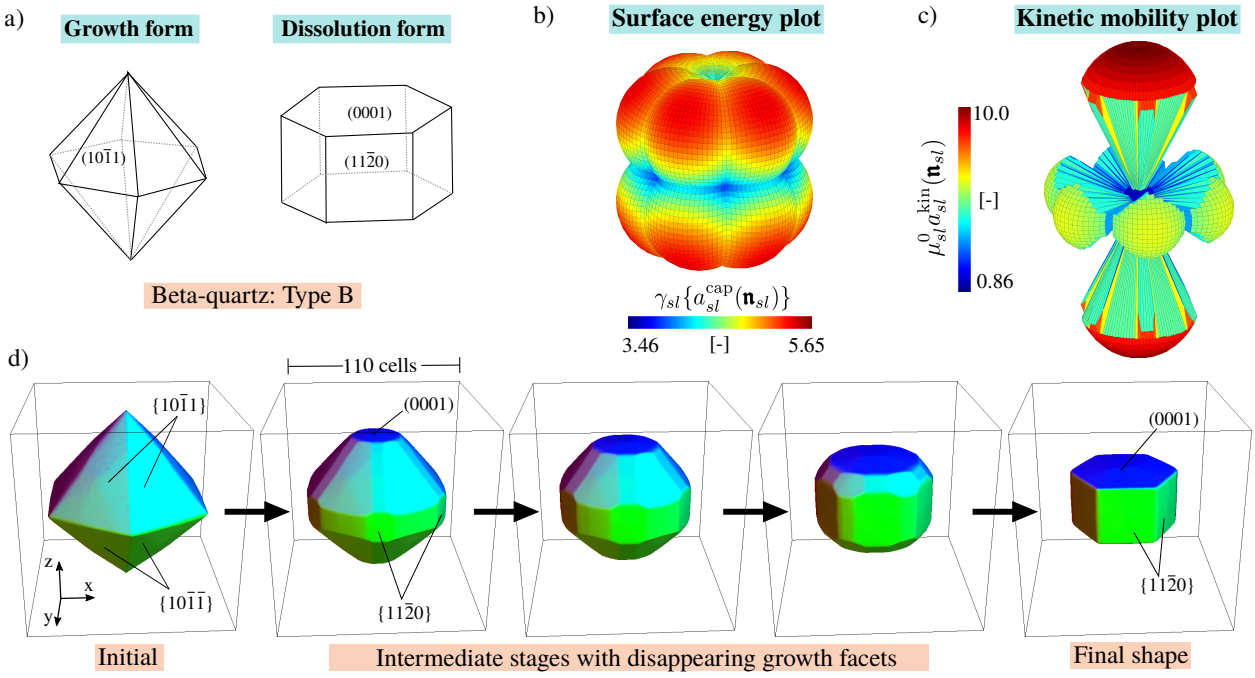

Figure 4: a) Growth and dissolution forms of Type B β-quartz (figure adapted from HEIMANN[14]). 3-D polar plots of b) surface energy and c) kinetic mobility of the interface. d) Simulated dissolution of Type B β-quartz crystal from its growth form. The progression is shown at representative stages. Different facets are shown in distinct colors for the sake of visualization.

Table 2: Obtained surface energies and chosen facet-specific anisotropy strength parameters of different facets for β-quartz.

Facets	c (0001), $(000\bar{1})$	m $\{11\bar{2}0\}$	d $\{10\bar{1}1\}$, $\{10\bar{1}\bar{1}\}$
Surface energy	γ_{sl}	$0.866\gamma_{sl}$	γ_{sl}
Anisotropy parameters	$\mathcal{A}_c = 0.991$	$\mathcal{A}_m = 0.995$	$\mathcal{A}_d = 1$

chosen, as listed in tables A3 and A4. The resulting polar plots of surface energy and kinetic mobility are depicted in figure 4b,c. The surface energy of facets obtained from the utilized vector set (in table A3) and the chosen anisotropy strength parameters (for the facet normal vectors in table A4) are given in table 2. In a cubic computational domain with an edge length of $110\Delta x$, a β-quartz crystal (colored) in its growth form embedded in a melt (transparent) was considered, see figure 4d (at the initial stage). Different stages of the simulated dissolution, using the phase-field parameter set given in table 1, are shown in the same figure. It is observed that the dissolution facets (0001), $(000\bar{1})$ and $\{11\bar{2}0\}$ appear at the corners of the growth forms. As the mobility of the dissolution facets is higher than the growth ones (i.e. d $\{10\bar{1}1\}$, $\{10\bar{1}\bar{1}\}$), they dissolve at faster rates. Thus, at later stages, the growth facets completely disappear. During the subsequent dissolution, the basal planes (0001) and $(000\bar{1})$ dissolve at faster rates than $\{11\bar{2}0\}$, due to higher kinetic mobilities of the former.

3.1.3 Dissolution of β-succinic acid

Experiments of Snyder et al.[25] reported that β-succinic acid crystals dissolve such that new faces appear at the edges of the growth form, see figure 5a,b. We refer to these dissolution faces as S-facets (terminology based on the PBC theory[18]). The S-facets with the miller indices $\{111\}$ dissolve faster as compared to those appearing on the lateral edges (i.e. faces with miller indices (031) and (110)). Thus, the final dissolution form (figure 5c) comprises only of the faster moving $\{111\}$ facets. Following our proposed prescription we chose the set of vertex vectors of the dissolution form to be given as an input for the capillary anisotropy

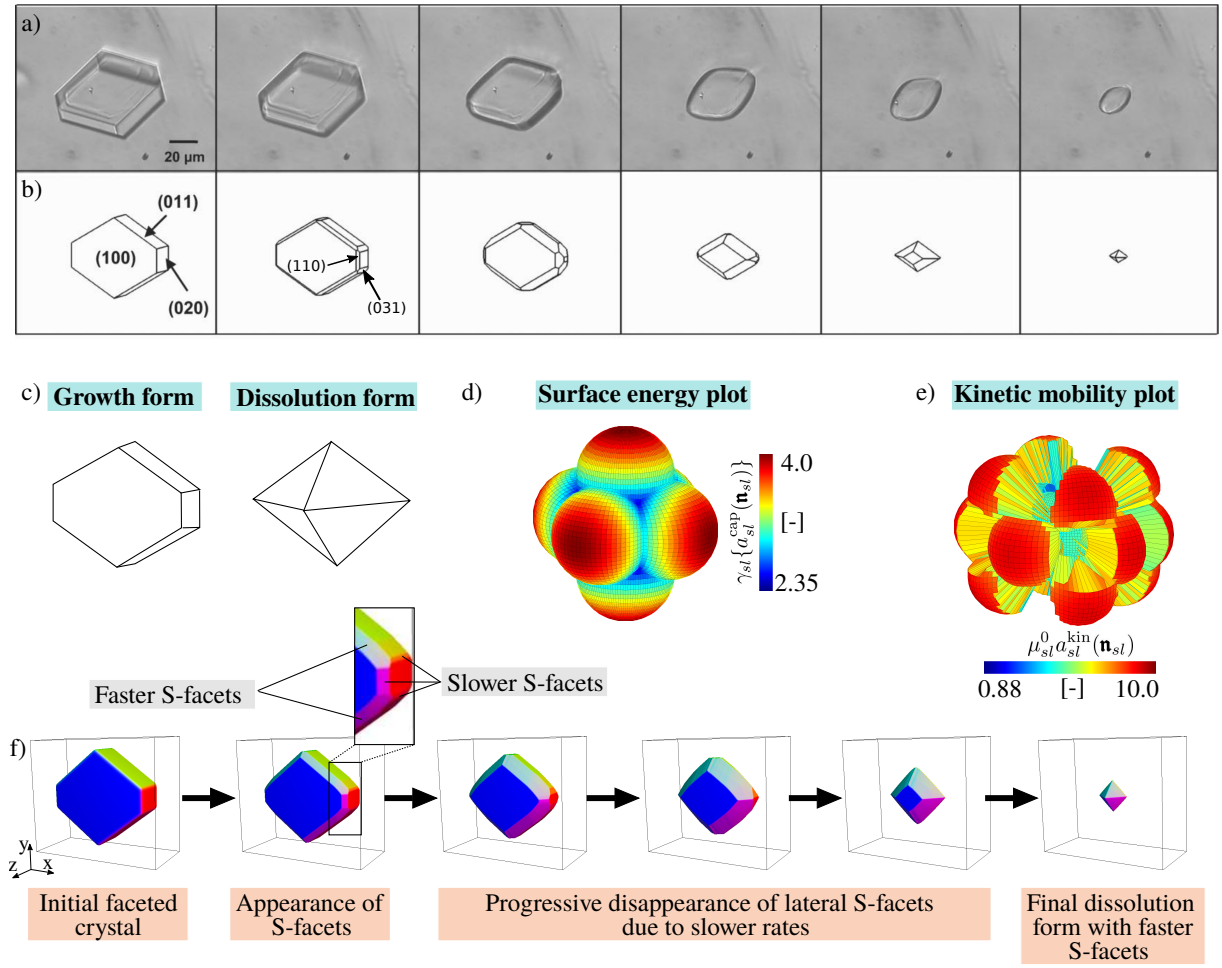

Figure 5: Faceted shape evolution of a β-succinic acid crystal during dissolution as reported by Snyder and Doherty [17] based on their a) experiment and their own b) a priori mathematical model (figure reprinted/adapted with permission from Snyder and Doherty.[17] Copyright 2008 American Chemical Society). c) Considered growth and dissolution forms of β-succinic acid. 3-D polar plots of d) surface energy and e) kinetic mobility. f) Different representative stages of the simulated dissolution. For the sake of visualization, different facets are shown in distinct colors, and the liquid phase as transparent in the rest of the computational domain.

function, as listed in table A5. The resulting polar plot of surface energy is shown in figure 5d, where the local minima represent the directions corresponding to {111} planes. For the kinetic anisotropy function, we chose the set of pairs of facet normal vectors given in table A6, accounting for the growth as well as different dissolution facets that appear during the process, as reported by Snyder et al..[25] In order to computationally imitate the order of precedence of different faces during the crystal shape evolution, different facets were assigned

Table 3: Obtained surface energies and chosen facet-specific anisotropy strength parameters of different facets for β-succinic acid.

Facets	{111}	(002), (00$\bar{2}$)	(020), (0$\bar{2}$0)	{011}	(031),(0$\bar{3}$1), (03$\bar{1}$),(0$\bar{3}\bar{1}$)
Surface energy	$0.5774\gamma_{sl}$	γ_{sl}	γ_{sl}	$0.7071\gamma_{sl}$	$0.9487\gamma_{sl}$
Anisotropy parameters	$\mathcal{A}_{111}$=0.991	$\mathcal{A}_{002}$=0.991	$\mathcal{A}_{020}$=0.995	$\mathcal{A}_{011}$=0.996	$\mathcal{A}_{031}$=0.991

different kinetic mobilities. The chosen set of facet-specific anisotropy strength parameters and the derived surface energies are given in table 3. The polar plot of the kinetic mobility is depicted in figure 5e. In a computational domain of size $110\Delta x \times 95\Delta x \times 50\Delta x$ filled with liquid phase, we simulate the dissolution of a single β-succinic acid crystal from its growth form, using the phase-field parameter set given in table 1. Figure 5f shows different stages of the simulated dissolution of the crystal (in rgb colors) dispersed in liquid (in the rest of the domain). As expected, different S-facets appear at the edges of the crystal, and dissolve according to their kinetic mobilities. At intermediate stages, the lateral S-faces disappear due to lower mobilities (for {011}) and higher surface energies (for {011} and (031) group) than those with miller indices {111}. It is worthy to note that, although the mobility of (002) facet is same as {111}; however, due to higher surface energy, the former also vanishes during the later stages. Hence, the final crystal shape contains only the fast moving and energetically most favorable {111} facets.

3.2 Quantitative modeling of dissolution of α-quartz

Using the physical conditions and the parameter set that was systematically determined in section 2.3, we quantitatively model the dissolution of α-quartz in a silica-undersaturated solution. The set of input model parameters along with the corresponding physical conditions are summarized in table 4, where the parameters without non-dimensional values were only utilized for calculating the dissolution driving force and interfacial kinetic coefficient in the modeling. The input parameters for the anisotropy functions are listed in tables A7 and A8. The resulting surface energies of different facets are given in table 5. The set

Table 4: Input model parameters for α-quartz dissolution

Model parameters	Symbol	Non-dim. value	Dim. value
Grid cell size	Δx	1	1 μm
Time step width	Δt	0.001	12.6 s
Quartz-water interface energy	γ_{qw}	4	0.36 J/m^2
Length scale parameter	ε	4	4 μm
Kinetic coefficient of quartz-water interface	μ^0_{qw}	1	8.79×10^{-16} m^4/J-s
Driving force for dissolution	$\Delta f^{\mathrm{Diss}}_{\mathrm{qw}}$	-0.299	-26881 J/m^3
Temperature	T		439 K
Pressure	p		1 atm
Equilibrium concentration of H_4SiO_4	$\mathfrak{c}^{\mathrm{eq}}_{\mathrm{H_4SiO_4}}$		385 ppm
Actual concentration of H_4SiO_4	$\mathfrak{c}_{\mathrm{H_4SiO_4}}$		193 ppm
Dissolution rate constant for quartz	k_+		2.09×10^{-6} 1/s
Molar volume of quartz	$V^{\mathrm{qtz}}_{\mathrm{m}}$		22.7×10^{-6} m^3
Molar volume of water	$V^{\mathrm{H_2O}}_{\mathrm{m}}$		18×10^{-6} m^3

$\boldsymbol{\mathcal{A}} = \{\mathcal{A}_m, \mathcal{A}_r, \mathcal{A}_d, \mathcal{A}_c, \mathcal{A}_a\}$ comprises of the facet-specific anisotropy strength parameters of the faces present in the growth (i.e. r and m) and dissolution (i.e. d and c) forms of α-quartz. Moreover, an additional parameter $\mathcal{A}_a$ was added to obviate the non-physical curvatures (concave surfaces) at certain interfacial points, otherwise occurring due to high mobility jumps. In order to precisely capture the anisotropic dissolution tendencies of α-quartz (discussed in section 2.3.4), the set $\boldsymbol{\mathcal{A}}$ was calibrated. We considered a computational domain of size 540 μm $\times$ 340 μm $\times$ 290 μm with an α-quartz crystal in its growth form, measuring 490 μm and 298 μm along the c- and a-axis, respectively (see figure 6a at the initial stage). For this numerical setup, numerous simulations of single crystal dissolution were performed by varying the parameters in the set $\boldsymbol{\mathcal{A}}$. For the values of the facet-specific anisotropy parameters as listed in table 5, the experimentally observed dissolution behav-

Table 5: Obtained surface energy and chosen facet-specific anisotropy strength parameters of different facets for α-quartz

Facets	c (0001), $(000\bar{1})$	d $\{11\bar{2}2\}$, $\{11\bar{2}\bar{2}\}$	r $\{10\bar{1}1\}$, $\{10\bar{1}\bar{1}\}$	m $\{10\bar{1}0\}$	Additional
Surface energy	γ_{qw}	γ_{qw}	$1.227\gamma_{\mathrm{qw}}$	$1.561\gamma_{\mathrm{qw}}$	$1.352\gamma_{\mathrm{qw}}$
Anisotropy parameters	$\mathcal{A}_c = 0.99625$	$\mathcal{A}_d = 0.9965$	$\mathcal{A}_r = 0.9994272$	$\mathcal{A}_m = 1.0$	$\mathcal{A}_a = 1.0$

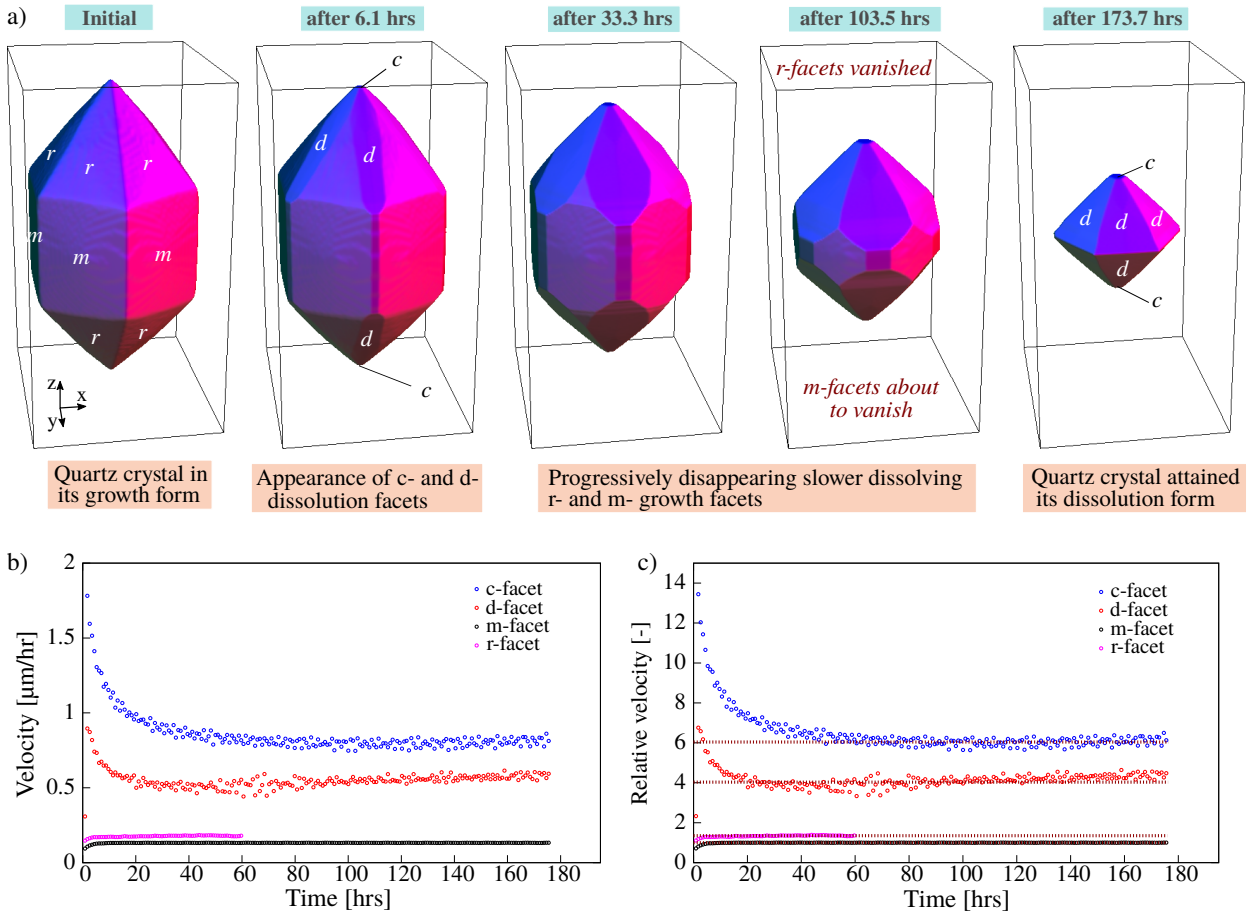

Figure 6: a) Simulated dissolution of α-quartz crystal in silica-undersaturated solution from its growth form. The progression is shown at representative stages. For the sake of visualization, different facets are shown in distinct colors and liquid phase as transparent in the rest of domain. Plots of b) absolute velocity and c) relative velocity (v/v_m) with respect to m-facet, as a function of time for different facets during dissolution.

ior of α-quartz (see section 2.3.4) was recovered. Figure 6a depicts different stages of the simulated dissolution. As expected, the dissolution facets are observed to appear at appropriate sites of the growth form, see figure 6a after 6.1 hrs. As the dissolution progresses, the growth facets begin to vanish due to their lower shift velocities and higher surface energies than the dissolution faces. Therefore, at later stages (after 173.7 hrs in figure 6a), only the faster moving and energetically favorable dissolution facets are sustained in the crystal shape. Figure 6b,c depicts the plots of temporal evolution of absolute and relative velocities (i.e. v/v_m, with respect to m-facet) for different facets. The simulated velocities of m- and

r-facets of $v_m = 0.132$ μm/hr and $v_r = 0.179$ μm/hr compare well with the estimated values of $v_m^{\text{exp}} = 0.11$ & 0.122 μm/hr and $v_r^{\text{exp}} = 0.151$ & 0.176 μm/hr in different alkali solutions in the dissolution experiments of Gratz and Bird,[39] at the $(p, \mathfrak{c}, T)$ conditions considered in the present modeling. Moreover, the simulated velocities of c- and d-facets of $v_c = 0.8$ μm/hr and $v_d = 0.534$ μm/hr, and thereby the relative velocities of $v_c/v_m \sim 6$ and $v_d/v_m \sim 4$, are in agreement with the previous literature,[18,21,32] as comprehensively discussed in section 2.3.4. We remark that in the present example, care has been taken in choosing the grid spacing such that large interface width artefacts are avoided. It is noteworthy that the present model exhibits dependencies on the initial size of crystal, i.e. the relative shift velocities of different facets vary for simulations of different-sized crystals dissolving from their growth form. Therefore, the anisotropy parameters determined in the present case correspond to the particular numerical setup considered in this work. Moreover, the complete simulation parameter set was determined based on an extensive review of different experimental works. Thus, we remark that the presented modeling and calibration procedure serve as a template for precisely capturing the dissolution behaviour of different crystalline solids in the phase-field model, when accurate data from experiments is available.

3.2.1 Dissolution of a single crystal sphere of α-quartz

Using the physical parameters (table 4) and the calibrated anisotropy parameters for α-quartz (tables 5, A7 and A8), we simulate the dissolution of a single crystal sphere (diameter: 200 μm) of α-quartz in a cubic computational domain of edge length 220 μm filled with the silica-undersaturated fluid. Figure 7 depicts the crystal shape evolution at different representative stages. As the incorporated anisotropy accounts for the facets present in growth (i.e. r and m) as well as dissolution form (i.e. c and d), all these faces appear during the intermediate stages (between 12.3 and 38.6 hours in figure 7). At later stages (i.e. after 63.2 hrs), the crystal shape exhibits the dissolution form with c and d-facets, due to higher shift velocities and lower surface energies of these planes. Dissolution experiments of single

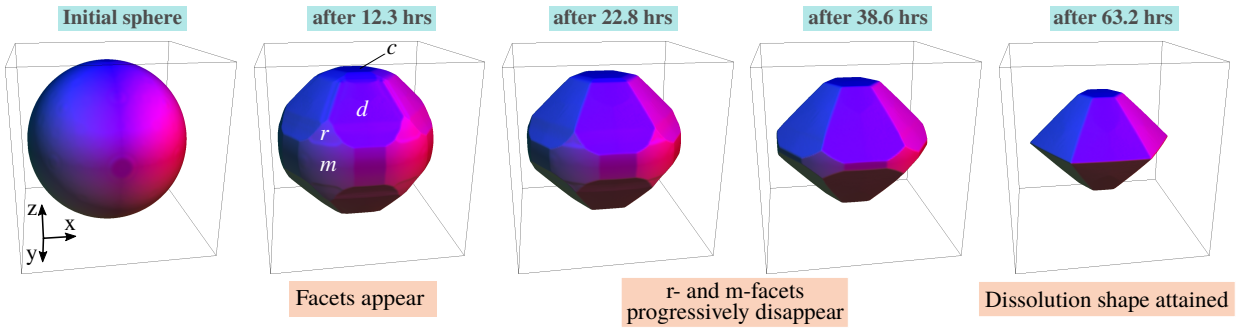

Figure 7: Simulated dissolution of a spherical crystal of α-quartz in silica-undersaturated solution. Progression is shown at representative stages. Different facets are shown in distinct colors for the sake of visualization.

crystal spheres of β-quartz in the NaF-$K_2S_2O_7$ melt reported three stages in the formation of a dissolution form, namely *sphere*, *edge* and *vertex* stage (Fig. 2 in Heimann[14]). In the present modeling of α-quartz dissolution, as we adopted the dissolution and growth forms corresponding to the above-mentioned experiments of β-quartz, our simulations are able to recreate these crystal shapes at different stages, i.e. edge stage (after 12.3 hrs) and vertex stage (after 38.6 hrs) starting from the initial sphere stage.

4 Conclusion and Outlook

In this work, we presented a thermodynamically consistent and generalized anisotropic phase-field model of faceted crystal dissolution. For capturing the shape evolution in the modeling, we proposed a novel and general prescription of input parameters that controls the anisotropies associated with the interface energy and kinetic mobility of the crystal surface. With this prescription, the model is able to simulate the dissolution of crystalline solids exhibiting distinct crystallographic facets in their growth and dissolution forms, as described by the Periodic bond chain (PBC) theory.[18] The prescription also allows to account for the occurrence of additional intermediate facets, if demanded by the physics of a specific crystal-liquid system. As a starting point, we validated the model by qualitatively simulating the dissolution of single crystals of different materials belonging to distinct crystal systems, in

two (2-D) as well as three-dimensions (3-D). From these validatory simulations, the following inferences were derived:

1. Numerical results of the dissolving 2-D hexagonal crystals elucidated that facets with lower interfacial energy and higher kinetic mobilities (and thereby higher shift velocities) are predominantly present in the crystal shape and are sustained at the later stages of dissolution, consistent with the well-known hypothesis of steady state dissolution shapes discussed in Snyder and Doherty,[17] and as also expected from the anisotropy prescription.

2. The simulated dissolution of a mineralogical crystal of β-quartz aptly captured the appearance of kinked faces and subsequent evolution into its dissolution form, in agreement with the experimental findings of Heimann.[14] These results also confirmed that the proposed prescription is straightforwardly applicable in 3-D as well.

3. In the third example, we simulated the dissolution of an organic crystal of β-succinic acid, illustrating the appearance of stepped facets at the edges of its growth form, as found in the previous experiments.[17] This example further demonstrated that by carefully modulating the energetics and kinetics of the crystal surface, on the basis of an appropriate selection of anisotropy parameters following the proposed prescription; the order of precedence and relative shift velocities of different facets can be adequately controlled in the present phase-field model.

Next, in order to elucidate the procedure to quantitatively simulate the faceted crystal dissolution process with this model, we considered the dissolution of α-quartz in silica-undersaturated solution at the experimental conditions of Gratz and Bird.[39] Further, based on an extensive literature review, the missing parameters were determined at the physical conditions matching (or close to) these experiments. The anisotropy parameters for α-quartz$-$water system were recovered by simulating the dissolution of single crystals from their growth form, and adjusting the relative dissolution rates of different facets to match the

values that were inferred after a comprehensive analysis of the previous literature.[18,21,32,40] From the simulation results of α-quartz dissolution with the complete parameter set, the following conclusions were drawn:

1. The shape evolution of an α-quartz crystal, initially in its growth form (with m and r facets), occurs such that, along with the dissolution of existing growth facets (as discussed in Ostapenko and Mitsyuk[46]), additional c and d faces appear and dissolve at different rates, as also expected from the determined input parameter set.

2. The numerically obtained absolute shift velocities of different facets match well with the values reported in the reference experiments.[40]

It is noteworthy that, as the growth and dissolution forms chosen for α-quartz were adopted from the shapes proposed by Heimann[14] for β-quartz; the different stages of formation of dissolution form reported for a dissolving spherical crystal in their experiments, were also recreated in our model predictions.

Present work serves as one of the very first phase-field investigations addressing the phenomenon of faceted crystal dissolution as described by the PBC theory. With the proposed novel prescription of anisotropy, a precise calibration of dissolution behavior was conveniently achieved for various crystal-liquid systems, as demonstrated in the numerical examples. However, we remark that various other forms for anisotropy functions may exist for capturing the dissolution tendencies in different systems. The scope of this work was restricted to modeling applications focussing on single crystal dissolution processes in different materials. However, we remark that the presented model can be readily applied to simulate dissolution in polycrystalline materials and sedimentary rocks. In such multigrain systems, additional complexities such as faster or slower dissolution along the grain boundaries, or presence of different types of grains (e.g. quartz and feldspar in sandstones) with their unique and distinct dissolution tendencies, can be incorporated. The present modeling assumes a constant

driving force of dissolution. This assumption is admissible when particle detachment is very slow compared to diffusion and advection. In systems where the above assumption breaks down, the model needs to be coupled with the equations of solute concentration as well as fluid-flow. To account for the motion and deformation of detached crystals, a further coupling with the equations of rigid body dynamics and solid mechanics could be considered. Thus, the present work paves the way for more advanced phase-field models of dissolution also accounting for the above-mentioned extensions.

5 Appendix

This section lists the input set of vectors for the capillary and kinetic anisotropy functions for the simulations showcased in the present work. In all the simulations, the anisotropy strength parameter of $\delta = 1000$ was set. Further, a list of all the symbols is given in the last part of this section.

5.1 Anisotropy parameters for the hexagonal growth and dissolution forms

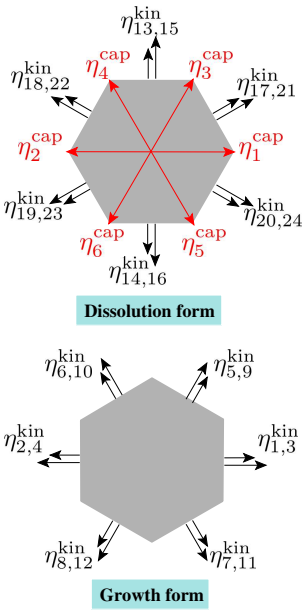

Figure A1: Hexagonal growth and dissolution forms illustrating the input vectors for the capillary and kinetic anisotropy corresponding to the vertices and facets of these forms.

	x	y
$\boldsymbol{\eta}^{cap}_{1,2}$	± 1.155	0
$\boldsymbol{\eta}^{cap}_{3..6}$	± 0.577	± 1

Table A1: Set of vertex vectors for capillary anisotropy function corresponding to the 2-D hexagonal dissolution form, as also schematically shown (in red color) in figure A1.

From growth form			From dissolution form		
	x	y		x	y
$\boldsymbol{\eta}^{kin}_{1,2}$	± 1	0	$\boldsymbol{\eta}^{kin}_{13,14}$	0	± 1
$\boldsymbol{\eta}^{kin}_{3,4}$	$\pm 1^{*}\mathcal{A}_1$	0	$\boldsymbol{\eta}^{kin}_{15,16}$	0	$\pm 1^{*}\mathcal{A}_3$
$\boldsymbol{\eta}^{kin}_{5..8}$	± 0.5	± 0.866	$\boldsymbol{\eta}^{kin}_{17..20}$	± 0.866	± 0.5
$\boldsymbol{\eta}^{kin}_{9..12}$	$\pm 0.5^{*}\mathcal{A}_2$	$\pm 0.866^{*}\mathcal{A}_2$	$\boldsymbol{\eta}^{kin}_{21..24}$	$\pm 0.866^{*}\mathcal{A}_4$	$\pm 0.5^{*}\mathcal{A}_4$

Table A2: Facet normal vectors for kinetic anisotropy function for 2-D hexagonal growth and dissolution forms, as also schematically shown (in black color) in figure A1.

5.2 Anisotropy parameters for Type B β-quartz

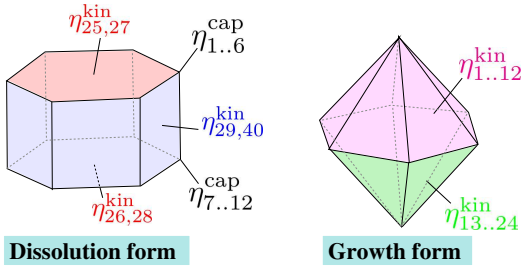

Figure A2: Growth and dissolution forms of β-quartz illustrating the input vectors for the capillary and kinetic anisotropy corresponding to the vertices and facets of these forms.

	x	y	z
$\boldsymbol{\eta}^{cap}_{1,2}$	± 1	0	1
$\boldsymbol{\eta}^{cap}_{3..6}$	± 0.5	± 0.866	1
$\boldsymbol{\eta}^{cap}_{7,8}$	± 1	0	-1
$\boldsymbol{\eta}^{cap}_{9..12}$	± 0.5	± 0.866	-1

Table A3: Set of vertex vectors for capillary anisotropy function corresponding to the β-quartz dissolution form, as also schematically shown (in black color) in figure A2.

Table A4: Facet normal vectors for kinetic anisotropy function for β-quartz growth and dissolution forms, as also schematically shown in figure A2.

	From growth form				From dissolution form		
	x	y	z		x	y	z
$\boldsymbol{\eta}^{\text{kin}}_{1..2}$	± 0.7857	0	0.6186	$\boldsymbol{\eta}^{\text{kin}}_{25,26}$	0	0	± 1
$\boldsymbol{\eta}^{\text{kin}}_{3..6}$	± 0.3929	± 0.6805	0.6186	$\boldsymbol{\eta}^{\text{kin}}_{27,28}$	0	0	$\pm 1{*}\mathcal{A}_c$
$\boldsymbol{\eta}^{\text{kin}}_{7..8}$	$\pm 0.7857{*}\mathcal{A}_d$	0	$0.6186{*}\mathcal{A}_d$	$\boldsymbol{\eta}^{\text{kin}}_{29,30}$	± 1	0	0
$\boldsymbol{\eta}^{\text{kin}}_{9..12}$	$\pm 0.3929{*}\mathcal{A}_d$	$\pm 0.6805{*}\mathcal{A}_d$	$0.6186{*}\mathcal{A}_d$	$\boldsymbol{\eta}^{\text{kin}}_{31,32}$	$\pm 1{*}\mathcal{A}_m$	0	0
$\boldsymbol{\eta}^{\text{kin}}_{13..14}$	± 0.7857	0	-0.6186	$\boldsymbol{\eta}^{\text{kin}}_{33..36}$	± 0.866	± 0.5	0
$\boldsymbol{\eta}^{\text{kin}}_{15..18}$	± 0.3929	± 0.6805	-0.6186	$\boldsymbol{\eta}^{\text{kin}}_{37..40}$	$\pm 0.866{*}\mathcal{A}_m$	$\pm 0.5{*}\mathcal{A}_m$	0
$\boldsymbol{\eta}^{\text{kin}}_{19..20}$	$\pm 0.7857{*}\mathcal{A}_d$	0	$-0.6186{*}\mathcal{A}_d$				
$\boldsymbol{\eta}^{\text{kin}}_{21..24}$	$\pm 0.3929{*}\mathcal{A}_d$	$\pm 0.6805{*}\mathcal{A}_d$	$-0.6186{*}\mathcal{A}_d$				

5.3 Anisotropy parameters for β-succinic acid

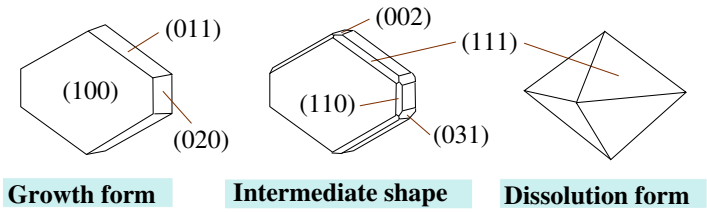

Figure A3: Growth and dissolution forms of β-succinic acid along with the intermediate shape with additional facets appearing during dissolution.

	x	y	z
$\boldsymbol{\eta}^{\text{cap}}_{1,2}$	± 1	0	0
$\boldsymbol{\eta}^{\text{cap}}_{3,4}$	0	± 1	0
$\boldsymbol{\eta}^{\text{cap}}_{5,6}$	0	0	± 1

Table A5: Set of vertex vectors for capillary anisotropy function corresponding to the β-succinic acid dissolution form.

Table A6: Facet normal vectors for kinetic anisotropy function for the growth and dissolution forms along with intermediate shape for β-succinic acid, as shown in figure A3. The subscript of each anisotropy strength parameter appearing in the components of a vector corresponds to the facet it belongs to.

	From growth form				From dissolution form				From intermediate shape		
	x	y	z		x	y	z		x	y	z
$\boldsymbol{\eta}^{\text{kin}}_{1,2}$	± 1	0	0	$\boldsymbol{\eta}^{\text{kin}}_{17..24}$	± 0.5774	± 0.5774	± 0.5774	$\boldsymbol{\eta}^{\text{kin}}_{33..36}$	± 0.9487	± 0.3162	0
$\boldsymbol{\eta}^{\text{kin}}_{3,4}$	$\pm 1{*}\mathcal{A}_{020}$	0	0	$\boldsymbol{\eta}^{\text{kin}}_{25..32}$	$\pm 0.5774{*}\mathcal{A}_{111}$	$\pm 0.5774{*}\mathcal{A}_{111}$	$\pm 0.5774{*}\mathcal{A}_{111}$	$\boldsymbol{\eta}^{\text{kin}}_{37..40}$	$\pm 0.9487{*}\mathcal{A}_{031}$	$\pm 0.3162{*}\mathcal{A}_{031}$	0
$\boldsymbol{\eta}^{\text{kin}}_{5,6}$	0	0	± 1					$\boldsymbol{\eta}^{\text{kin}}_{41..44}$	± 0.7071	0	± 0.7071
$\boldsymbol{\eta}^{\text{kin}}_{7,8}$	0	0	$\pm 1{*}\mathcal{A}_{100}$					$\boldsymbol{\eta}^{\text{kin}}_{45..48}$	$\pm 0.7071{*}\mathcal{A}_{101}$	0	$\pm 0.7071{*}\mathcal{A}_{101}$
$\boldsymbol{\eta}^{\text{kin}}_{9..12}$	± 0.7071	± 0.7071	0					$\boldsymbol{\eta}^{\text{kin}}_{49..52}$	0	± 0.7071	± 0.7071
$\boldsymbol{\eta}^{\text{kin}}_{13..16}$	$\pm 0.7071{*}\mathcal{A}_{011}$	$\pm 0.7071{*}\mathcal{A}_{011}$	0					$\boldsymbol{\eta}^{\text{kin}}_{53..56}$	0	$\pm 0.7071{*}\mathcal{A}_{011}$	$\pm 0.7071{*}\mathcal{A}_{011}$
								$\boldsymbol{\eta}^{\text{kin}}_{57,58}$	0	± 1	0
								$\boldsymbol{\eta}^{\text{kin}}_{59,60}$	0	$\pm 1{*}\mathcal{A}_{002}$	0

5.4 Anisotropy parameters for α-quartz

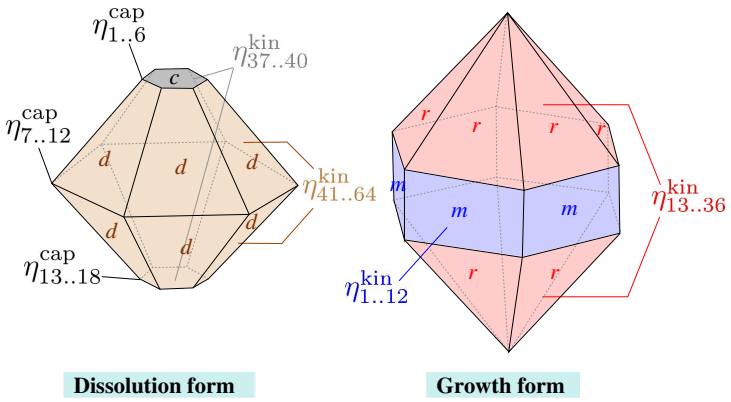

Figure A4: Growth and dissolution forms of α-quartz illustrating the subscript-numbering of the input vectors for the capillary and kinetic anisotropy corresponding to the vertices and facets of these forms.

	x	y	z
$\boldsymbol{\eta}^{cap}_{1,2}$	±0.5105	0	1
$\boldsymbol{\eta}^{cap}_{3..6}$	±0.2552	±0.4421	1
$\boldsymbol{\eta}^{cap}_{7,8}$	±1.5612	0	0
$\boldsymbol{\eta}^{cap}_{9..12}$	±0.7806	±1.352	0
$\boldsymbol{\eta}^{cap}_{13,14}$	±0.5105	0	-1
$\boldsymbol{\eta}^{cap}_{15..18}$	±0.2552	±0.4421	-1

Table A7: Set of vertex vectors for capillary anisotropy function corresponding to the α-quartz dissolution form.

Table A8: Facet normal vectors for kinetic anisotropy function for the growth and dissolution forms along with additional vectors (to avoid non-physical curvatures) for α-quartz, as also schematically shown in figure A4.

From growth form				From dissolution form				Additional vectors			
	x	y	z		x	y	z		x	y	z
$\boldsymbol{\eta}^{kin}_{1,2}$	±1	0	0	$\boldsymbol{\eta}^{kin}_{37,38}$	0	0	±1	$\boldsymbol{\eta}^{kin}_{65..68}$	0	±1	±0.22
$\boldsymbol{\eta}^{kin}_{3,4}$	±1*$\mathcal{A}_m$	0	0	$\boldsymbol{\eta}^{kin}_{39,40}$	0	0	±1*$\mathcal{A}_c$	$\boldsymbol{\eta}^{kin}_{69..72}$	0	±1*$\mathcal{A}_a$	±0.22*$\mathcal{A}_a$
$\boldsymbol{\eta}^{kin}_{5..8}$	±0.5	±0.866	0	$\boldsymbol{\eta}^{kin}_{41..44}$	0	±0.74	±0.6727	$\boldsymbol{\eta}^{kin}_{73..80}$	±0.866	±0.5	±0.22
$\boldsymbol{\eta}^{kin}_{9..12}$	±0.5*$\mathcal{A}_m$	±0.866*$\mathcal{A}_m$	0	$\boldsymbol{\eta}^{kin}_{45..48}$	0	±0.74*$\mathcal{A}_d$	±0.6727*$\mathcal{A}_d$	$\boldsymbol{\eta}^{kin}_{81..88}$	±0.866*$\mathcal{A}_a$	±0.5*$\mathcal{A}_a$	±0.22*$\mathcal{A}_a$
$\boldsymbol{\eta}^{kin}_{13..16}$	±0.7857	0	±0.6186	$\boldsymbol{\eta}^{kin}_{49..56}$	±0.6408	±0.37	±0.6727				
$\boldsymbol{\eta}^{kin}_{17..20}$	±0.7857*$\mathcal{A}_r$	0	±0.6186*$\mathcal{A}_r$	$\boldsymbol{\eta}^{kin}_{57..64}$	±0.6408*$\mathcal{A}_d$	±0.37*$\mathcal{A}_d$	±0.6727*$\mathcal{A}_d$				
$\boldsymbol{\eta}^{kin}_{21..28}$	±0.3929	±0.6805	±0.6186								
$\boldsymbol{\eta}^{kin}_{29..36}$	±0.3929*$\mathcal{A}_r$	±0.6805*$\mathcal{A}_r$	±0.6186*$\mathcal{A}_r$								

5.5 List of Symbols

Complete list of symbols corresponding to all the physical and model parameters used in this work is given in table A9.

6 Supplementary material

The attached animation videos were generated from the digital data sets of the simulated dissolution in different crystalline solids that were reported in this work. These data sets

Table A9: List of Symbols. $(\cdot)$ denotes the place-holder for one phase, $(\cdot\cdot)$ is the place-holder for two phases and $(*)$ represents the place-holder for a facet.

Model parameters	Symbol	Subscript of phase $(\cdot)$	Symbol
Phase-field variable of phase $(\cdot)$	$\phi_{(\cdot)}$	solid	s
Phase-field duplet	$\boldsymbol{\phi}$	liquid	l
Physical domain	Ω	quartz	q
Grid cell size	Δx	water	w
Time step width	Δt	Subscript of two phases $(\cdot\cdot)$	
Bulk region of phase $(\cdot)$	$\mathcal{B}_{(\cdot)}$	solid-liquid	sl
Diffuse interface region between phases $(\cdot\cdot)$	$\mathcal{I}_{(\cdot\cdot)}$	quartz-water	qw
Helmholtz free energy	$\mathcal{F}$	α-Quartz specific model parameters	
Bulk free energy contribution	$\mathcal{F}_{\text{bulk}}$	Temperature	T
Interface free energy contribution	$\mathcal{F}_{\text{interface}}$	Pressure	p
Bulk free energy density	$\mathfrak{f}_{\text{bulk}}$	Difference of molar volume	ΔV
Interface free energy density	$\mathfrak{f}_{\text{interface}}$	Change of Gibbs free energy	ΔG
Free energy density of phase $(\cdot)$	$\mathfrak{f}_{(\cdot)}$	Gas constant	R
Potential energy density	ω/ε	Saturation index	$\mathcal{S}$
Gradient energy density	εa	Equilibrium concentration of H_4SiO_4	$\mathfrak{c}^{\text{eq}}_{H_4SiO_4}$
Length scale parameter	ε	Actual concentration of H_4SiO_4	$\mathfrak{c}_{H_4SiO_4}$
Surface energy of $(\cdot\cdot)$ interface	$\gamma_{(\cdot\cdot)}$	Dissolution rate constant for quartz	k_+
Capillary anisotropy function	$a^{\text{cap}}_{(\cdot\cdot)}$	Molar volume of quartz	$V_{\text{m}}^{\text{qtz}}$
Phase-field gradient vector	$\mathbf{q}_{(\cdot\cdot)}$	Molar volume of water	$V_{\text{m}}^{\text{H}_2\text{O}}$
Unit phase-field gradient vector	$\mathfrak{n}_{(\cdot\cdot)}$	Velocity of qw interface	v_{qw}
Kinetic mobility of $(\cdot\cdot)$ interface	$\mu_{(\cdot\cdot)}$	Velocity of m, r, d, c-facet	$v_{(*)}$
Kinetic coefficient of $(\cdot\cdot)$ interface	$\mu^0_{(\cdot\cdot)}$		
Kinetic anisotropy function of $(\cdot\cdot)$ interface	$a^{\text{kin}}_{(\cdot\cdot)}$		
Capillary anisotropy vector set	$\boldsymbol{\mathcal{N}}^{\text{cap}}$		
k^{th} Capillary anisotropy vector	$\boldsymbol{\eta}^{\text{cap}}_k$		
Kinetic anisotropy vector set	$\boldsymbol{\mathcal{N}}^{\text{kin}}$		
k^{th} Kinetic anisotropy vector	$\boldsymbol{\eta}^{\text{kin}}_k$		
Full set of anisotropy strength parameters	$\hat{\boldsymbol{\mathcal{A}}}$		
Reduced set of anisotropy strength parameters	$\boldsymbol{\mathcal{A}}$		
Facet specific anisotropy strength parameter	$\mathcal{A}_{(*)}$		
Driving force for dissolution	$\Delta f^{\text{Diss}}_{(\cdot\cdot)}$		

can be accessed in the general-purpose open-access data repository at Prajapati et al..[83] The data sets were generated using the multiphysics software framework PACE3D (VERSION 2.5.1). The software license can be bought at Steinbeis Network (www.steinbeis.de) in the management of Prof. Dr. rer. nat. Britta Nestler and Dr.-Ing. Michael Selzer under the subject area “Material Simulation and Process Optimization".

Acknowledgments

NP and MSe are thankful to the Helmholtz Association for the financial support through the program "Renewable Energies (RE)", efficient use of geothermal energy 35.14.01. MSp thanks the funding support by the German Research Foundation (DFG) through the project NE 822/34-1. The authors are grateful to Dr. rer. nat. Benjamin Busch and Prof. Dr. rer. nat. habil. Christoph Hilgers for the conceptual discussions that benefitted this research work.

References

(1) Hayes, J. B. Sandstone diagenesis – the hole truth. *Soc. Econ. Paleontologists Mineralogists, Spec. Publ.; USA; DA*. **1979**, *26*, 127–139

(2) Pye, K.; Krinsley, D. Formation of secondary porosity in sandstones by quartz framework grain dissolution. *Nature* **1985**, *317* (6032), 54–56.

(3) Scott, S. W.; Driesner, T. Permeability changes resulting from quartz precipitation and dissolution around upper crustal intrusions. *Geofluids* **2018**.

(4) Tran, M. K.; Shin, H.; Byun, Y.-H.; Lee, J.-S. Mineral dissolution effects on mechanical strength. *Engineering Geology* **2012**, *125*, 26–34.

(5) Yim, M.-S.; Murty, K. L. Materials issues in nuclear-waste management. *Jom* **2000**, *52* (9), 26–29.

(6) Nitschke, F. Numerical and Experimental Characterization of Dissolution and Precipitation Processes in Deep Geothermal Reservoirs. *Ph.D. thesis, Karlsruher Institut für Technologie (KIT)*, **2018**, 35.14.01; LK 01.

(7) Donohoe, K. G.; Turner, T. R.; Jackson, K. A. Etching Processes in Semiconductor Manufacturing. *Materials Science and Technology*, **2013**.

(8) Edwards, L. The dissolution and diffusion of aspirin in aqueous media. *Transactions of the Faraday Society* **1951**, *47*, 1191–1210.

(9) Dokoumetzidis, A.; Macheras, P. A century of dissolution research: from Noyes and Whitney to the biopharmaceutics classification system. *International Journal of Pharmaceutics* **2006**, *321* (1-2), 1–11.

(10) Simone, E. Crystal engineering approaches for the food industry, in:*Physics in Food Manufacturing*; IOP Publishing, **2020**; 7-1 – 7-27.

(11) Singh, M. R.; Nere, N.; Tung, H.-H.; Mukherjee, S.; Bordawekar, S.; Ramkrishna, D. Measurement of polar plots of crystal dissolution rates using hot-stage microscopy. Some further insights into dissolution morphologies. *Crystal Growth & Design* **2014**, *14* (11), 5647–5661.

(12) Lacmann, R.; Franke, W.; Heimann, R. The dissolution forms of single crystal spheres: I. Theory for the molecular-kinetics interpretation. *Journal of Crystal Growth* **1974**, *26* (1), 107–116.

(13) Moore, M. On the shapes of dissolved crystals. *Mineralogical Magazine* **1986**, *50* (356), 331–332.

(14) Heimann, R. Dissolution forms of single crystal spheres of quartz in acid alkali fluoride melts. *Journal of Crystal Growth* **1973**, *18* (1), 61–69.

(15) Gibbs, J. W. *The scientific papers of J. Willard Gibbs*; Longmans, Green and Company, **1906**; Vol. 1.

(16) Lovette, M. A.; Browning, A. R.; Griffin, D. W.; Sizemore, J. P.; Snyder, R. C.; Doherty, M. F. Crystal shape engineering. *Industrial & Engineering Chemistry Research* **2008**, *47* (24), 9812–9833.

(17) Snyder, R. C.; Doherty, M. F. Faceted crystal shape evolution during dissolution or growth. *AIChE Journal* **2007**, *53* (5), 1337–1348.

(18) Hartman, P.; Perdok, W. On the relations between structure and morphology of crystals. I. *Acta Crystallographica* **1955**, *8* (1), 49–52.

(19) Hartman, P.; Perdok, W. On the relations between structure and morphology of crystals. II. *Acta Crystallographica* **1955**, *8* (9), 521–524.

(20) Hartman, P.; Perdok, W. On the relations between structure and morphology of crystals. III. *Acta Crystallographica* **1955**, *8* (9), 525–529.

(21) Hurst, A. R. A scale of dissolution for quartz and its implications for diagenetic processes in sandstones. *Sedimentology* **1981**, *28* (4), 451–459.

(22) Morse, J. W.; Arvidson, R. S.; Lüttge, A. Calcium carbonate formation and dissolution. *Chemical Reviews* **2007**, *107* (2), 342–381.

(23) Yuan, K.; Starchenko, V.; Lee, S. S.; De Andrade, V.; Gursoy, D.; Sturchio, N. C.; Fenter, P. Mapping three-dimensional dissolution rates of calcite microcrystals: Effects of surface curvature and dissolved metal ions. *ACS Earth and Space Chemistry* **2019**, *3* (5), 833–843.

(24) Rimstidt, J. D. Diffusion control of quartz and forsterite dissolution rates. *Applied Geochemistry* **2015**, *61*, 99–108.

(25) Snyder, R. C.; Veesler, S.; Doherty, M. F. The evolution of crystal shape during dissolution: predictions and experiments. *Crystal Growth & Design* **2008**, *8* (4), 1100–1101.

(26) The quartz page. `http://www.quartzpage.de/gen_mod.html`, Accessed: 2020-11-02.

(27) Goldschmidt, V. *Atlas der Kristallformen*; C. Winter, **1922**; Vol. 7.

(28) Guthrie Jr, G. D.; Heaney, P. J. Mineralogical characteristics of silica polymorphs in relation to their biological activities. *Scandinavian Journal of Work, Environment & Health* **1995**, 5–8.

(29) The mineral and gemstone kingdom. available at: `https://www.minerals.net/quartz_polymorphs.aspx`, Accessed: 2020-11-02.

(30) Rimstidt, J. D.; Barnes, H. The kinetics of silica-water reactions. *Geochimica et Cosmochimica Acta* **1980**, *44* (11), 1683–1699.

(31) Castagliola, M.; Tellier, C.; Vaterkowski, J. Topography of etched rhombohedral faces of quartz crystals: evidence for orientation effects. *Journal of Materials Science* **1986**, *21* (10), 3551–3560.

(32) Liepmann, M. J. *Chemical durability of crystalline and vitreous oxides in alkaline solutions*; **1986**.

(33) Blum, A. E.; Yund, R. A.; Lasaga, A. C. The effect of dislocation density on the dissolution rate of quartz. *Geochimica et Cosmochimica Acta* **1990**, *54* (2), 283–297.

(34) Dove, P. M.; Crerar, D. A. Kinetics of quartz dissolution in electrolyte solutions using a hydrothermal mixed flow reactor. *Geochimica et Cosmochimica Acta* **1990**, *54* (4), 955–969.

(35) Brady, P. V.; Walther, J. V. Kinetics of quartz dissolution at low temperatures. *Chemical Geology* **1990**, *82*, 253–264.

(36) Gratz, A. J.; Bird, P.; Quiro, G. B. Dissolution of quartz in aqueous basic solution, 106–236 C: Surface kinetics of "perfect" crystallographic faces. *Geochimica et Cosmochimica Acta* **1990**, *54* (11), 2911–2922.

(37) Tester, J. W.; Worley, W. G.; Robinson, B. A.; Grigsby, C. O.; Feerer, J. L. Correlating quartz dissolution kinetics in pure water from 25 to 625 ^{o}C. *Geochimica et Cosmochimica Acta* **1994**, *58* (11), 2407–2420.

(38) Gratz, A.; Manne, S.; Hansma, P. Atomic force microscopy of atomic-scale ledges and etch pits formed during dissolution of quartz. *Science* **1991**, *251* (4999), 1343–1346.

(39) Gratz, A. J.; Bird, P. Quartz dissolution: Negative crystal experiments and a rate law. *Geochimica et Cosmochimica Acta* **1993**, *57* (5), 965–976.

(40) Gratz, A. J.; Bird, P. Quartz dissolution: Theory of rough and smooth surfaces. *Geochimica et Cosmochimica Acta* **1993**, *57* (5), 977–989.

(41) Worley, W.; Tester, J.; Grigsby, C. Quartz dissolution kinetics from 100–200° C as a function of pH and ionic strength. *AIChE Journal* **1996**, *42* (12), 3442–3457.

(42) Dove, P. M.; Nix, C. J. The influence of the alkaline earth cations, magnesium, calcium, and barium on the dissolution kinetics of quartz. *Geochimica et Cosmochimica Acta* **1997**, *61* (16), 3329–3340.

(43) Jendoubi, F.; Mgaidi, A.; Maaoui, M. E. The dissolution kinetics of sand as function of particle size. *The Canadian Journal of Chemical Engineering* **1998**, *76* (2), 233–238.

(44) Gautier, J.-M. An experimental study of quartz precipitation and dissolution rates at 200 C. *MinM* **1998**, *62* (1), 509–510.

(45) Dove, P. M.; Han, N.; De Yoreo, J. J. Mechanisms of classical crystal growth theory explain quartz and silicate dissolution behavior. *Proceedings of the National Academy of Sciences* **2005**, *102* (43), 15357–15362.

(46) Ostapenko, G.; Mitsyuk, B. Asymmetry of growth and dissolution on basal, minor rhombohedral and prism faces of quartz. *Journal of Crystal Growth* **2006**, *294* (2), 330–338.

(47) Stack, A. G.; Raiteri, P.; Gale, J. D. Accurate rates of the complex mechanisms for growth and dissolution of minerals using a combination of rare-event theories. *Journal of the American Chemical Society* **2012**, *134* (1), 11–14.

(48) Nangia, S.; Garrison, B. J. Advanced Monte Carlo approach to study evolution of quartz surface during the dissolution process. *Journal of the American Chemical Society* **2009**, *131* (27), 9538–9546.

(49) Zhang, L.; Lüttge, A. Morphological evolution of dissolving feldspar particles with anisotropic surface kinetics and implications for dissolution rate normalization and grain size dependence: A kinetic modeling study. *Geochimica et Cosmochimica Acta* **2009**, *73* (22), 6757–6770.

(50) Osher, S.; Sethian, J. A. Fronts propagating with curvature-dependent speed: algorithms based on Hamilton-Jacobi formulations. *Journal of Computational Physics* **1988**, *79* (1), 12–49.

(51) van Noorden, T. L. Crystal precipitation and dissolution in a porous medium: effective equations and numerical experiments. *Multiscale Modeling & Simulation* **2009**, *7* (3), 1220–1236.

(52) Ray, N.; Oberlander, J.; Frolkovic, P. Numerical investigation of a fully coupled micro-macro model for mineral dissolution and precipitation. *Computational Geosciences* **2019**, *23* (5), 1173–1192.

(53) Snyder, R. C.; Studener, S.; Doherty, M. F. Manipulation of crystal shape by cycles of growth and dissolution. *AIChE Journal* **2007**, *53* (6), 1510–1517.

(54) Molins, S.; Soulaine, C.; Prasianakis, N. I.; Abbasi, A.; Poncet, P.; Ladd, A. J.; Starchenko, V.; Roman, S.; Trebotich, D.; Tchelepi, H. A. Simulation of mineral dissolution at the pore scale with evolving fluid-solid interfaces: review of approaches and benchmark problem set. *Computational Geosciences* **2020**, 1–34.

(55) Ankit, K.; Nestler, B.; Selzer, M.; Reichardt, M. Phase-field study of grain boundary tracking behavior in crack-seal microstructures. *Contributions to Mineralogy and Petrology* **2013**, *166* (6), 1709–1723.

(56) Ankit, K.; Selzer, M.; Hilgers, C.; Nestler, B. Phase-field modeling of fracture cementation processes in 3-D. *J Pet Sci Res* **2015**, *4*, 79–96.

(57) Ankit, K.; Urai, J. L.; Nestler, B. Microstructural evolution in bitaxial crack-seal veins: A phase-field study. *Journal of Geophysical Research: Solid Earth* **2015**, *120* (5), 3096–3118.

(58) Wendler, F.; Okamoto, A.; Blum, P. Phase-field modeling of epitaxial growth of polycrystalline quartz veins in hydrothermal experiments. *Geofluids* **2016**, *16* (2), 211–230.

(59) Prajapati, N.; Selzer, M.; Nestler, B. Computational modeling of calcite cementation in saline limestone aquifers: a phase-field study. *Geothermal Energy* **2017**, *5* (1), 1–15.

(60) Prajapati, N.; Selzer, M.; Nestler, B.; Busch, B.; Hilgers, C. Modeling fracture cementation processes in calcite limestone: a phase-field study. *Geothermal Energy* **2018**, *6* (1), 1–15.

(61) Prajapati, N.; Selzer, M.; Nestler, B.; Busch, B.; Hilgers, C.; Ankit, K. Three-dimensional phase-field investigation of pore space cementation and permeability in quartz sandstone. *Journal of Geophysical Research: Solid Earth* **2018**, *123* (8), 6378–6396.

(62) Prajapati, N.; Abad Gonzalez, A.; Selzer, M.; Nestler, B.; Busch, B.; Hilgers, C. Quartz Cementation in Polycrystalline Sandstone: Insights From Phase-Field Simulations. *Journal of Geophysical Research: Solid Earth* **2020**, *125* (2), e2019JB019137.

(63) Spruženiece, L.; Späth, M.; Urai, J. L.; Ukar, E.; Selzer, M.; Nestler, B.; Schwedt, A.

Formation of wide-blocky calcite veins by extreme growth competition. *Journal of the Geological Society* **2020**.

(64) Spruženiece, L.; Späth, M.; Urai, J. L.; Ukar, E.; Selzer, M.; Nestler, B. Wide-blocky veins explained by dependency of crystal growth rate on fracture surface type: Insights from phase-field modeling.: Insights from phase-field modelling. *Geology* **2021**.

(65) Chen, L.-Q. Phase-field models for microstructure evolution. *Annual review of materials research* **2002**, *32* (1), 113–140.

(66) Moelans, N.; Blanpain, B.; Wollants, P. An introduction to phase-field modeling of microstructure evolution. *Calphad* **2008**, *32* (2), 268–294.

(67) Qin, R.; Bhadeshia, H. Phase field method. *Materials Science and Technology* **2010**, *26* (7), 803–811.

(68) Nestler, B.; Choudhury, A. Phase-field modeling of multi-component systems. *Current Opinion in Solid State and Materials Science* **2011**, *15* (3), 93–105.

(69) Krill, C. E. *Handbook of Materials Modeling*; Springer, **2005**, 2157–2171.

(70) Chen, L.-Q. Phase-field method of phase transitions/domain structures in ferroelectric thin films: a review. *Journal of the American Ceramic Society* **2008**, *91* (6), 1835–1844.

(71) Spatschek, R.; Brener, E.; Karma, A. Phase field modeling of crack propagation. *Philosophical Magazine* **2011**, *91* (1), 75–95.

(72) Aihara, S.; Takaki, T.; Takada, N. Multi-phase-field modeling using a conservative Allen–Cahn equation for multiphase flow. *Computers & Fluids* **2019**, *178*, 141–151.

(73) Xu, Z.; Meakin, P. Phase-field modeling of solute precipitation and dissolution. *The Journal of Chemical Physics* **2008**, *129* (1), 014705.

(74) Xu, Z.; Huang, H.; Li, X.; Meakin, P. Phase field and level set methods for modeling solute precipitation and/or dissolution. *Computer Physics Communications* **2012**, *183* (1), 15–19.

(75) Bringedal, C.; von Wolff, L.; Pop, I. S. Phase field modeling of precipitation and dissolution processes in porous media: Upscaling and numerical experiments. *Multiscale Modeling & Simulation* **2020**, *18* (2), 1076–1112.

(76) Nestler, I.; Garcke, H.; Stinner, B. Multicomponent alloy solidification: phase-field modeling and simulations. *Physical Review E* **2005,** *71* (4), 041609.

(77) Steinbach, I. Phase-field models in materials science. *Modelling and Simulation in Materials Science and Engineering* **2009**, *17* (7), 073001.

(78) Schoof, E. Chemomechanische Modellierung der Wärmebehandlung von Stählen mit der Phasenfeldmethode. *PhD Thesis, Karlsruher Institut für Technologie (KIT)* **2020**.

(79) Pace3D. `https://www.hs-karlsruhe.de/en/research/hska-research-institutions/institute-for-digital-materials-science-idm/pace-3d-software`, Accessed: 2020-11-02.

(80) Hötzer, J.; Reiter, A.; Hierl, H.; Steinmetz, P.; Selzer, M.; Nestler, B. The parallel multi-physics phase-field framework Pace3D. *Journal of Computational Science* **2018**, *26*, 1–12.

(81) Parks, G. A. Surface and interfacial free energies of quartz. *Journal of Geophysical Research: Solid Earth* **1984**, *89* (B6), 3997–4008.

(82) The quartz page. `http://www.quartzpage.de/crs_habits.html`, Accessed: 2020-11-02.

(83) Prajapati, N.; Späth, M.; Knecht, L.; Selzer, M.; Nestler, B. Numerical data sets pertaining to phase-field simulations of faceted crystal dissolution processes [Data set] *Zenodo* **2020**, `http://doi.org/10.5281/zenodo.4317382`.